Applied Radiation and Isotopes 69 (2011) 1721–1724

Contents lists available at ScienceDirect

Applied Radiation and Isotopes

journal homepage: www.elsevier.com/locate/apradiso

Boron neutron capture therapy for clear cell sarcoma (CCS): Biodistribution study of *p*-borono-L-phenylalanine in CCS-bearing animal models

T. Andoh [a], T. Fujimoto [b], T. Sudo [c], I. Fujita [b], M. Imabori [b], H. Moritake [d], T. Sugimoto [e], Y. Sakuma [f], T. Takeuchi [g], S. Kawabata [h], M. Kirihata [i], T. Akisue [j], K. Yayama [k], M. Kurosaka [j], S. Miyatake [h], Y. Fukumori [a], H. Ichikawa [a,*]

[a] *Laboratory of Pharmaceutical Technology, Faculty of Pharmaceutical Sciences and Cooperative Research Center of Life Sciences, Kobe Gakuin University, Kobe 650-8586, Japan*
[b] *Department of Orthopaedic Surgery, Hyogo Cancer Center, Akashi 673-0021, Japan*
[c] *Section of Translational Research, Hyogo Cancer Center, Akashi 673-0021, Japan*
[d] *Department of Pediatrics, Miyazaki University, Kiyotake 889-1692, Japan*
[e] *Department of Pediatrics, Saiseikai Shigaken Hospital, Ritto 520-3046, Japan*
[f] *Department of Pathology, Hyogo Cancer Center, Akashi 673-0021, Japan*
[g] *Department of Pathology, Kochi University, Nangoku 783-8505, Japan*
[h] *Department of Neurosurgery, Osaka Medical College, Osaka 569-8686, Japan*
[i] *Graduate School of Life and Environmental Sciences, Osaka Prefecture University, Sakai 599-8531, Japan*
[j] *Department of Orthopaedic Surgery, Kobe University Graduate School of Medicine, Kobe 650-0017, Japan*
[k] *Laboratory of Cardiovascular Pharmacology, Faculty of Pharmaceutical Sciences and Cooperative Research Center of Life Sciences, Kobe Gakuin University, Kobe 650-8586, Japan*

ARTICLE INFO

Available online 1 March 2011

Keywords:
Biodistribution
p-Borono-L-phenylalanine
Clear cell sarcoma
MP-CCS-SY
Boron neutron capture therapy
Anti-BPA monoclonal antibody

ABSTRACT

Clear cell sarcoma (CCS) is a rare melanocytic malignant tumor with a poor prognosis. Our previous study demonstrated that *in vitro* cultured CCS cells have the ability to highly uptake L-BPA and thus boron neutron capture therapy could be a new option for CCS treatment. This paper proved that a remarkably high accumulation of ^{10}B (45–74 ppm) in tumor was obtained even in a CCS-bearing animal with a well-controlled biodistribution followed by intravenous administration of L-BPA-fructose complex (500 mg BPA/kg).

1. Introduction

Clear cell sarcoma (CCS), a rare melanocytic malignant tumor with a predilection for young adults, is of poor prognosis. Since its treatment other than surgical resection is lacking, a new clinical approach for its management is required (Weiss and Goldblum, 2001).

Melanoma cells preferentially take up *p*-borono-L-phenylalanine (L-BPA) because its chemical structure is similar to tyrosine required for melanogenesis. Therefore, L-BPA has been used in boron neutron capture therapy (BNCT) for malignant melanoma (Mishima et al., 1989). CCS is also capable of producing melanin. Similarity in melannogensis between melanoma and CCS promises high BPA uptake by CCS. Indeed, we have proved that remarkable uptake of BPA with an extremely high level, i.e., 80 μg ^{10}B/g cells, took place when CCS was exposed to BPA-containing cell culture medium *in vitro* (Fujimoto et al., in press). Thus, BNCT using L-BPA is expected to be a new clinical option for the treatment of CCS, provided that such a high accumulation of boron in CCS can be realized even in vivo under a well-controlled biodistribution of L-BPA.

In the present study, we are aiming at investigating *in vivo* biodistribution of L-BPA in a CCS-bearing animal model. For this purpose, CCS cell line of human origin (MP-CCS-SY) was employed and a CCS-bearing animal model was established by subcutaneous transplantation of MP-CCS-SY to nude mice. Biodistribution of L-BPA followed by its intravenous administration into the CCS-bearing nude mice thus obtained was evaluated. Additionally, the tumor resected from the BPA-given mice was assessed with immunohistological examination using anti-BPA monoclonal antibody to visualize microscopic distribution of BPA in the tumor tissue.

2. Materials and methods

2.1. Chemicals

L-BPA (^{10}B enriched) was kindly supplied by Stella Pharma Corporation (Osaka, Japan). Fructose, perchloric acid ($HClO_4$, 60%),

* Corresponding author. Tel.: +81 78 974 1551; fax: +81 78 974 4814.
E-mail address: ichikawa@pharm.kobegakuin.ac.jp (H. Ichikawa).

0969-8043/$ - see front matter © 2011 Elsevier Ltd. All rights reserved.
doi:10.1016/j.apradiso.2011.02.005

hydrogen peroxide (H_2O_2, 30%) and boron standard solution (1000 μg/mL) were purchased from Nacalai Tesque, Inc. (Kyoto, Japan). L-BPA was used as a fructose complex (BPA-Fr, 4000 μg ^{10}B/mL) (Yoshino et al., 1989). Anti-BPA monoclonal antibody (anti-BPA MAb) was obtained as a self-made product (Kirihata and Asano 2008). LSAB2 kit/HRP (DAB) was purchased from DAKO Japan, Inc. (Kyoto, Japan).

2.2. Cell

The MP-CCS-SY established from the bone metastatic tissue of a 17-years-old girl was employed as a human CCS cell line (Moritake et al., 2002). The melanogenesis of MP-CCS-SY has been reported previously: the melanosome was identified by electron-microscopic appearance and indirect immunofluoresence for melanoma-associated antigens (Moritake et al., 2002). The MP-CCS-SY cells were cultured in RPMI-1640 medium containing penicillin (100 U/mL), streptomycin (100 μg/mL) and 10% heat-inactivated fetal bovine serum, and incubated in a humidified atmosphere of 5% CO_2 in air at 37 °C.

2.3. Animal and tumor

All animal experiments were performed according to the regulations of the Animal Care and Use Committee of Kobe Gakuin University (Kobe, Japan). Four-weeks-old female BALB/cAJcl-nu/nu nude mice (body weight of approx. 15 g) were purchased from CLEA Japan, Inc. In order to establish CCS-bearing animal models, 0.1 mL of the culture medium containing 1×10^7 MP-CCS-SY cells was subcutaneously (s.c.) implanted into the dorsal or femoral region of the nude mice. These two models were used in biodistibution studies of L-BPA.

2.4. Biodistribution of BPA-Fr

When the MP-CCS-SY tumor in each mouse (body weight of approximately 20 g) grew to about 10 mm in diameter (approximately four weeks after MP-CCS-SY cells implantation), BPA-Fr (500 mg BPA/kg) was intravenously (i.v.) administered via

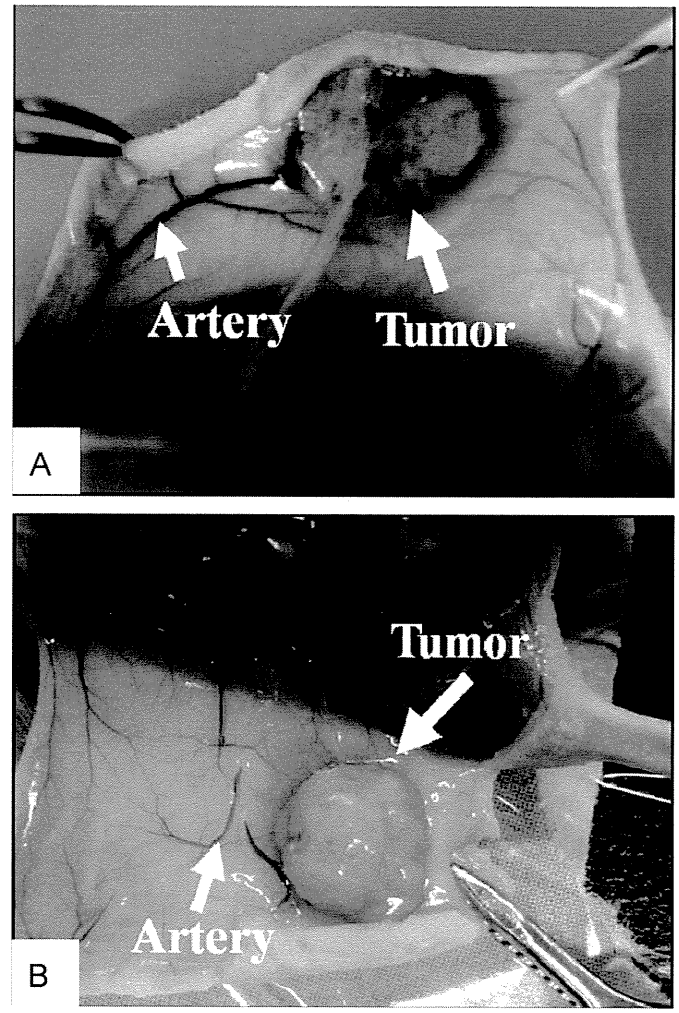

Fig. 2. Photographs showing CCS formation in dorsal region (A, Fujimoto et al., in press) and femoral region (B) of nude mice. Significant angiogenesis can be seen especially in the dorsal region.

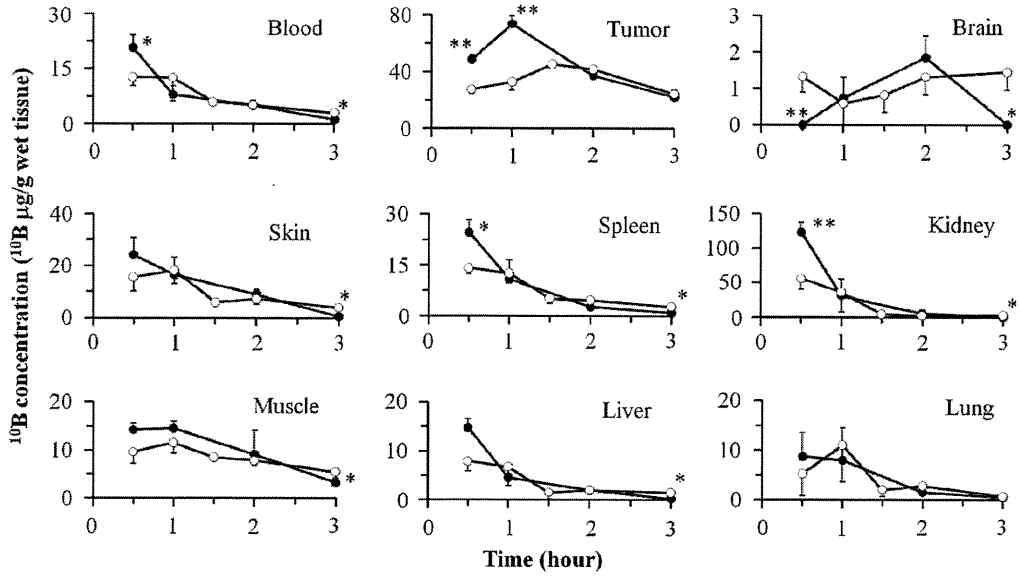

Fig. 1. Time course changes of ^{10}B concentration in tissues after i.v. administration of BPA-Fr (500 mg BPA/kg) to nude mice having MP-CCS-SY in dorsal region (●) and those in femoral region (○). *: $p < 0.05$, **: $p < 0.01$, significantly different from the ^{10}B concentration of dorsal region. Each value represents the mean ± S.D. ($n=3$).

femoral vein to each tumor-bearing nude mouse under anesthesia with diethyl ether. At predetermined time intervals after dosing, blood sample was collected by cardiac puncture under deep anesthesia and then residual blood in the organs was removed by saline perfusion. Subsequently, the nude mice were sacrificed with diethyl ether. Tissue samples including the liver, spleen, kidney, lung, brain and tumor were collected immediately, washed with saline and lightly blotted to remove any excess blood and water. The skin and muscle were collected from the nates of the mice. The liver, kidney, brain and tumor were homogenized by a high-speed homogenizer.

2.5. Histological evaluation

The tumor mass was resected from the dorsally MP-CCS-SY-bearing nude mouse sacrificed one hour after intravenous administration of BPA-Fr (500 mg BPA/kg) under anesthesia with diethyl ether. This mass was routinely processed by fixation in formalin for overnight at 20–23 °C and then embedded in paraffin. Serial tissue sections were cut from the paraffin block, placed on glass slides and dried overnight. A part of the sections was stained with hematoxylin–eosin (H.E.) according to standard protocols for histological examination. Separately, some of the sections were incubated with anti-BPA Mab, stained with LSAB2 kit/HRP (DAB) and then counterstained with hematoxylin by the procedure described in the literature (Nakagawa, 2006) to visualize microscopic distribution of L-BPA in the tumor tissues.

2.6. Determination of boron

Quantitative determination of boron was carried out by the inductively coupled plasma atomic emission spectrometric (ICP-AES) method. A weighed sample of tissues or homogenates (typically 100–200 mg) was hermetically digested with $HClO_4$ (0.6 mL) and H_2O_2 (1.2 mL) for 48 h at 75°C. The resulting solution was diluted with ultra pure water to be 5 mL in total volume, followed by filtration with a 0.45 μm disposable filter unit. Boron concentration in each sample was determined by ICP-AES (SPS 3100, SII NanoTechnology Inc., Tokyo, Japan). The emission intensity was measured at 249.773 nm. The calibration curve obtained from dilutes of the boron standard solution (1000 μg/mL) was linear in the range of 0.2–10 μg/mL.

3. Results and discussion

The biodistribution data of boron after i.v. administration of BPA-Fr (500 mg BPA/kg) are shown in Fig. 1. As a general tendency, the boron concentrations in blood, spleen, kidney, liver and skin decreased rapidly after i.v. administration of BPA-Fr. The peak boron concentrations did not exceed 25 μg $^{10}B/g$ in the liver, spleen, brain, lung, muscle and skin, while the transiently high boron concentration was found in kidney. In contrast, the boron concentration in tumor increased rapidly, peaked at 1 or 1.5 hours, and subsequently decayed with time. The peak concentration reached 74 μg $^{10}B/g$ wet tumor tissue (ppm) for dorsally tumor-bearing mice and 45 ppm for femorally tumor-bearing mice, respectively (Fig. 1). This concentration was higher than the minimum effective concentration of boron, i.e., 20–30 μg $^{10}B/g$ (Barth et al., 1992) in BNCT. Such a high boron concentration in the CCS-bearing animals would be attributable to a high cell-uptake and/or cell-affinity of L-BPA (Fujimoto et al., in press).

The dorsally tumor-bearing mice showed significantly higher peak boron concentrations in tumor, compared with the femorally tumor-bearing mice (Fig. 1). As represented in Fig. 2, the CCS in dorsal region resulted in somewhat more distinct angiogenesis than the CCS in femoral region. This difference in the extent of angiogenesis may account for the higher boron concentration in dorsally tumor-bearing mice.

Both tumor-to-blood (T/B) and tumor-to-skin (T/S) ratios should be large enough in order to avoid radiobiological damage to the normal skin. The T/B and T/S ratios at 1 hour after administration of BPA-Fr in dorsally tumor-bearing mice were 9.2 and 4.5, respectively, while those at 1.5 hour after administration of

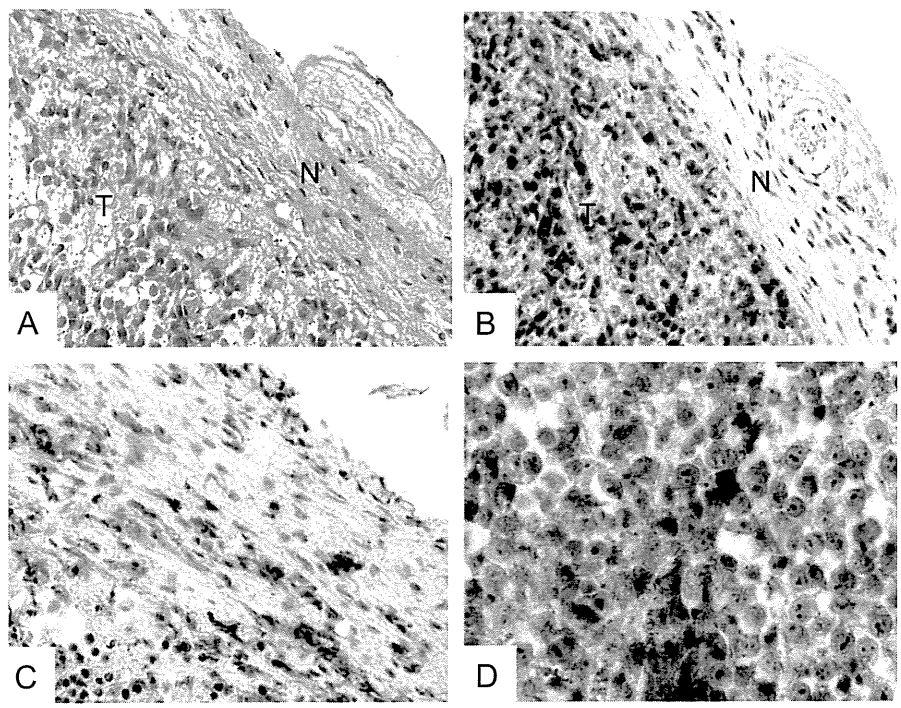

Fig. 3. Micrographs (100 ×) showing tumor sections (T) with the surrounding normal tissues (N) resected from BPA-administered mice (A, B, D) and non-BPA-administered mice (negative control, C). A: Hematoxylin-Eosin staining; B-D: immunostaining with anti-BPA MAb. D represents a magnified image (× 400) of B.

BPA-Fr in femorally tumor-bearing mice were 7.6 and 7.8, respectively. Previous experimental and clinical studies suggested that these ratios have to be at least 3 (Barth et al., 1996). The values of T/B and T/S obtained in the present study fulfill the therapeutic requirements.

H.E. staining data revealed that CCS tumor tissues were histologically different from the surrounding normal tissues, as evidenced from Fig. 3A. Fig. 3B–D shows the results of immunostaining with anti-BPA MAb. Here, the presence of BPA can be detected by browny coloration of tissues. The accumulation of BPA indicated by brownish color was predominant in the tumor tissues over the surround normal tissues (Fig. 3B), and tumor tissues obtained without BPA administration (negative control) did not develop brownish color well (Fig. 3C), suggesting that BPA is likely to be distributed in a CCS-selective manner. Interestingly, BPA was detected mainly in intracellular regions of CCS as seen in the magnified photograph (Fig. 3D). This can be a strong indication of cellular uptake of BPA taking place even *in vivo* CCS-bearing animals. Further studies are warranted to determine whether melanin synthesis is related to the high accumulation of boron in CCS.

4. Conclusions

Biodistribution of boron after i.v. administration of BPA-Fr into newly established CCS-bearing nude mice was studied. The peak concentrations of boron in tumor varied from 45 to 74 ppm, depending on the animal models. The T/B and T/S ratios were 9.2 and 4.5 in dorsally tumor bearing model, and 7.6 and 7.8 in femorally tumor bearing model, respectively. Tumor-specific BPA distribution was microscopically observed in the intravenously BPA-Fr-given CCS-bearing mice through immunohistological examination. A preclinical BNCT trial using a CCS-bearing mouse will be a next issue to clarify whether BNCT using BPA-Fr can be a promising therapeutic option for the CCS.

Acknowledgments

This work was supported in part by a Grant-in-Aid for Scientific Research (No. 22591657) from Japan Society for the Promotion of Science.

References

Barth, R.F., Soloway, A.H., Fairchild, R.G., Brugger, R.M., 1992. BNCT for cancer-realities and prospects. Cancer 70, 2995–3007.

Barth, R.F., Soloway, A.H., Brugger, R.M., 1996. Boron neutron capture therapy of brain tumors: past history, current status and future potential. Cancer Invest. 14, 534–560.

Fujimoto, T., Andoh, T., Sudo, T., Fujita, I., Imabori, M., Moritake, H., Sugimoto, T., Sakuma, Y., Takeuchi, T., Sonobe, H., Epstein, A.L., Akisue, T., Kirihata, M., Kurosaka, M., Fukumori, Y., Ichikawa, H. Evaluation of BPA uptake in clear cell sarcoma (CCS) *in vitro* and development of an *in vivo* model of CCS for BNCT studies. Appl. Radiat. Isots., in press, doi:10.1016/j.apradiso.2011.02.006.

Kirihata, M., Asano, T., 2008. JP Patent Pending 2008-94729.

Mishima, Y., Honda, C., Ichihashi, M., Obara, H., Hiratsuka, J., Fukuda, H., Karashima, H., Kobayashi, T., Kanda, K., Yoshino, K., 1989. Treatment of malignant-melanoma by single thermal-neutron capture therapy with melanoma-seeking B-10-compound. Lancet 12, 388–389.

Moritake, H., Sugimoto, T., Asada, Y., Yoshida, A.M., Maehara, Y., Epstein, L.A., Kuroda, H., 2002. Newly established clear cell sarcoma (malignant melanoma of soft parts) cell line expressing melanoma-associated Melan-A antigen and overexpressing C-MYC oncogene. Cancer Genet. Cytogenet. 135, 48–56.

Nakagawa, N., 2006. Therapeutic effect of boron neutron capture therapy on malignant glioma: fundamental studies using C6 rat glioma models. Med. J. Kinki Univ. 31, 215–224.

Weiss, S.W., Goldblum, J.R., 2001. Enzinger and Weiss's Soft Tissue Tumors, fourth ed., pp. 1240–1250.

Yoshino, K., Suzuki, A., Mori, Y., Kakihana, H., Honda, C., Mishima, Y., Kobayashi, T., Kanda, K., 1989. Improvement of solubility of p-boronophenylalanine by complex formation with monosaccharides. Strahlenther. Onkol. 165, 127–129.

J Neurooncol (2011) 105:423–431
DOI 10.1007/s11060-011-0610-9

CLINICAL STUDY – PATIENT STUDY

The distribution of vascular endothelial growth factor-producing cells in clinical radiation necrosis of the brain: pathological consideration of their potential roles

Naosuke Nonoguchi · Shin-Ichi Miyatake · Motoi Fukumoto · Motomasa Furuse · Ryo Hiramatsu · Shinji Kawabata · Toshihiko Kuroiwa · Motomu Tsuji · Manabu Fukumoto · Koji Ono

Received: 21 January 2011 / Accepted: 22 May 2011 / Published online: 18 June 2011

Abstract The cell type and localization of vascular endothelial growth factor (VEGF)-producing cells in human radiation necrosis (RN) are investigated from a histopathological and immunohistochemical standpoint using clinical specimens. Eighteen surgical specimens of symptomatic RN in the brain were retrospectively reviewed. These cases included different original histological tumor types and were treated with different radiation modalities. Histological analyses were performed using hematoxylin and eosin (H&E) staining, and anti-VEGF and anti-hypoxia-inducible factor (HIF)-1α immunohistochemistry. H&E staining showed marked angiogenesis and reactive astrocytosis at the perinecrotic area. The most prominent vasculature in this area was identified as telangiectasis. Immunohistochemistry indicated that HIF-1α was expressed predominantly in the perinecrotic area and that a large majority of VEGF-expressing cells were reactive astrocytes intensively distributed in this area. VEGF produced by the reactive astrocytes localized mainly in the perinecrotic area might be a major cause of both angiogenesis and the subsequent perilesional edema typically found in RN of the brain. The benefits of anti-VEGF antibody (bevacizumab) treatment in RN may be that VEGF secretion from the perinecrotic tissue is inhibited and that surgery would remove this tissue; both of these benefits result in effective reduction of edema associated with RN.

Keywords Angiogenesis · Bevacizumab · Boron neutron capture therapy · Hypoxia-inducible factor-1α · Radiation necrosis · Vascular endothelial growth factor

Introduction

White matter necrosis, demyelination, and vascular damage in the central nervous system (CNS) are the major dose-limiting side-effects in radiation therapy, not only for intracranial neoplasms but also for neoplasms of the head and neck region.

Histopathologically, the changes in vasculatures associated with radiation necrosis (RN) are largely degenerative or dystrophic, and feature telangiectasis, hyaline thickening of vessels, and fibrinoid necrosis with intravascular thromboses. Pathophysiologically, RN is characterized by increased permeability and disruption of the blood–brain barrier [1]. It is thought that such radiation vasculopathy may account for sporadic focal ischemia and/or microbleeding, and that, in later stages (weeks to years after radiation exposure), it may lead to a progressive mass effect with severe perilesional edema that can result in

Electronic supplementary material The online version of this article (doi:10.1007/s11060-011-0610-9) contains supplementary material, which is available to authorized users.

N. Nonoguchi · S.-I. Miyatake (✉) · M. Furuse · R. Hiramatsu · S. Kawabata · T. Kuroiwa
Department of Neurosurgery, Osaka Medical College, Takatsuki, Japan
e-mail: neu070@poh.osaka-med.ac.jp

M. Fukumoto · M. Fukumoto
Department of Pathology, Institute of Development, Aging and Cancer, Tohoku University, Sendai, Japan

M. Tsuji
Department of Clinical Pathology, Osaka Medical College, Takatsuki, Japan

K. Ono
Particle Radiation Oncology Research Center, Research Reactor Institute, Kyoto University, Kumatori, Japan

aggravation of symptoms in patients. Thus, the delayed necrosis of the brain following exposure to high doses of radiation should be recognized as a hazard.

New radiation therapies with high absorbed doses within tumor tissue, such as intensity-modulated radiation therapy, particle radiation therapy, and boron neutron capture therapy (BNCT), have recently been used to treat patients with malignant brain tumors, including glioblastoma (GB). High-dose radiation treatments may have potential for greater rates of tumor control [2–6], but this is typically at the expense of greater rates of RN within the treatment volume. Also, stereotactic radiosurgery (SRS) achieves good control over metastatic brain tumors with the risk of RN [7]. Medical therapy is often started first and surgery reserved for use only if the lesion is refractory, unless there is an increase in symptomatic intracranial pressure [8, 9]. In some cases, however, removal of only the center of the necrotic core does not result in rapid shrinkage of edema (personal experience and data not shown). Recently, bevacizumab, an anti-vascular endothelial growth factor (VEGF) antibody, has been recognized as a novel potential tool for treatment of RN [10–12], as we also reported [13]. This allowed us to understand the primary factors in the critical exacerbation of RN. However, it has been unclear what kinds of cells mainly produce and secrete VEGF as a target of bevacizumab or where the VEGF-producing cells exist in the brain with symptomatic RN. Thus, no report has clearly described the extent of surgical resection that is necessary and sufficient to educe the maximal therapeutic effect of surgical resection of necrotic tissue.

To identify the origin of VEGF in RN and to obtain answers to the questions above, we retrospectively reviewed clinical specimens of symptomatic RN by hematoxylin and eosin (H&E) staining and immunohistological analyses of VEGF and hypoxia-inducible factor (HIF)-1α, especially from the standpoint of the occurrence of angiogenesis and perilesional edema in RN. We also summarize the results of surgical treatment and bevacizumab treatment for symptomatic RN.

Patients and methods

Patients

From June 2004 to December 2009, a total of 27 symptomatic RN cases was treated at Osaka Medical College (Table 1). In this period, a total of 27 symptomatic RN cases were treated at this institute. They were treated mainly by S.-I.M., and were followed up for at least 1 month with medical treatment, including mainly oral steroids, anticoagulants, vitamin E, and others. Pathological examination of the original tumor revealed various histological types, including GB, metastatic brain tumor, and malignant meningioma, and also head and neck cancer. All patients were treated with intensive radiation therapy including proton particle radiation, SRS or tumor-targeting particle radiation (BNCT) [5, 14] with or without fractionated X-ray treatment. Table 1 lists the use of preceding radiotherapy in recurrent cases and chemotherapeutic agents just prior to onset of symptomatic RN.

Preoperative diagnosis of RN was performed by fluoride-18-labeled boronophenylalanine positron emission tomography (F-BPA-PET), as reported previously [14, 15]. Even if PET analysis suggested the lesion was RN, it did not exclude the possibility that a small quantity of living tumor cells remained in or around the lesion. In other words, PET determination as RN means that RN should be the major cause of radiographic enhancement and perilesional edema. For cases 1–18, the MRI-enhanced area was surgically excised with the aid of 5-aminolevulinic acid (ALA) [16, 17]. All 18 cases showed massive necrosis on H&E staining, which proved that PET as described above accurately diagnosed RN. All other cases (cases 19–27) received only conservative medical treatment. Six recent cases (cases 16, 23–27) were treated with bevacizumab. In one of these cases, necrotic foci were surgically excised initially and treated again with bevacizumab when recurrence of RN was observed (case 16). All patients were followed up with periodic computed tomography (CT) or magnetic resonance imaging (MRI). Neuroimaging revealed intralesional or perilesional bleeding in four cases (cases 8, 13, 20, and 22).

Histological and immunohistological analyses

Specimens from 18 cases with surgically removed necrotic masses underwent histological examination. Of the 18 surgical specimens that had sufficient volume for immunohistological analyses, 11 were preserved and analyzed for VEGF expression using anti-VEGF antibody (1:200 dilution; A-20; Santa Cruz Biotechnology, Santa Cruz, CA). Briefly, sections were deparaffinized and nonspecific binding was blocked with 1% nonfat milk and 0.1% Triton X. Immunohistochemistry was performed in an automatic stainer using the I-VIEW DAB universal kit according to the manufacturer's protocol (Ventana Medical Systems, Tucson, AZ, USA).

In addition, anti-HIF-1α (1:50 dilution; monoclonal mouse anti-human HIF-1α, clone H1alpha67; Novus Biologicals, Littleton, CO, USA) immunohistological analysis was applied in these 11 cases.

Table 1 Patient profile of symptomatic radiation necrosis

Case	Age (years)	Gender	KPS[a] (preop.)	KPS[b] (postop.)	Original dis.	Radiation[c]	Duration[d]	Steroids[e]	Chemotherapy
Surgical cases (excision for enhanced area on MRI)									
Case 1[f]	78	M	70	90	Sal. Duc. Ca.	XRT (NA), BNCT ×2 (6.1, 10.1 Gy-Eq)	20	4→0	–
Case 2[g]	73	F	60	60	GB	XRT (60 Gy), BNCT (11.7 Gy-Eq)	3	3→1	ACNU
Case 3	48	M	50	40	GB	SRS (20 Gy), BNCT (12.4 Gy-Eq)	12	8→1	ACNU, TMZ
Case 4	64	F	60	80	GB	BNCT (9.7 Gy-Eq), XRT (30 Gy)	12	4→0	–
Case 5	40	F	50	50	GB	BNCT (15.7 Gy-Eq), XRT (50 Gy)	8	2→0	TMZ
Case 6	57	M	50	70	GB	XRT (60 Gy), BNCT (13.6 Gy-Eq)	8	8→2	ACNU
Case 7	73	F	80	80	GB	BNCT (13.1 Gy-Eq), XRT (30 Gy)	8	2→0	–
Case 8[i]	42	M	60	70	GB	SRS (20 Gy), XRT (63 Gy)	8	4→2	ACNU
Case 9	57	F	70	80	Metastasis (Ade. Ca.)	SRS (22 Gy)	9	4→0	Herceptin
Case 10	28	F	60	60	MM	SRS ×2 (20, 15 Gy), BNCT ×2 (10.1, 10.2 Gy-Eq)	12	4→2	–
Case 11	61	F	60	60	MM	SRS (40 Gy), BNCT (8.7 Gy-Eq)	8	2→2	–
Case 12	23	F	60	60	GB	BNCT (10.8 Gy-Eq), XRT (50 Gy)	16	4→2	–
Case 13[i]	48	M	60	40	GB	XRT (60 Gy), BNCT (13.7 Gy-Eq)	5	5→4	PCV
Case 14	42	M	60	60	GB	XRT (60 Gy), BNCT (12.7 Gy-Eq)	5	4→4	PCV
Case 15	26	F	80	90	GB	BNCT (12.6 Gy-Eq), XRT (30 Gy)	14	4→2	–
Case 16[h]	53	F	70	80	GB	Proton (50 Gy-Eq), XRT (40 Gy)	5	4→1	ACNU
Case 17[f]	47	F	80	90	Ade. Ca.	XRT (NA), BNCT ×2 (NA)	7	6→0	–
Case 18	55	M	90	90	Metastasis (Ade. Ca.)	XRT (30 Gy), SRS (18 Gy)	11	4→0	–
Nonsurgical cases (treated medically)									
Case 19[f]	72	F	60	90	Ade. Ca.	XRT (NA), BNCT ×4 (NA)	6	2→0	–
Case 20[i]	58	F	90	100	GB	BNCT (11.5 Gy-Eq), XRT (40 Gy)	5	2→0	TMZ
Case 21	37	F	80	90	AA	XRT (50 Gy), SRS (10 Gy)	5	6→1	TMZ
Case 22[i]	73	M	90	70	GB	BNCT (12.2 Gy-Eq), XRT (30 Gy),	6	2→2	TMZ
Case 23[h]	58	F	50	80	Metastasis (LC Ade. Ca.)	XRT (30 Gy), SRS (30 Gy)	6	4→0	–
Case 24[h]	39	M	90	100	GB	BNCT (11.9 Gy-Eq), XRT (20 Gy)	10	4→0	TMZ
Case 25[h]	56	F	60	60	MM	XRT (50 Gy), SRS (32 Gy), BNCT (12.5 Gy-Eq)	12	2→2	–
Case 26	74	F	70	70	Metastasis (LC Ade. Ca.)	SRS (22 Gy)	24	4→0	–
Case 27[h]	55	M	80	90	Metastasis (LC small)	SRS (22.5 Gy)	18	1→0	CDDP, VP-16

ACNU nimustin, *TMZ* temozolomide, *PCV* procarbazine, nimustin, vincristin, *AA* anaplastic astrocytoma, *CDDP* cisplatinum, *VP-16* etoposide, *dis* disease

[a] *KPS* Karnofsky performance score assessed just prior to the treatment

[b] *KPS* Karnofsky performance score assessed at 1 month after the initiation of the treatment

[c] *XRT* X-ray treatment, *BNCT* boron neutron capture therapy, *SRS* stereotactic radiosurgery, *Gy-Eq* biologically equivalent X-ray dose that would have equivalent effects on tumor and on normal brain. In BNCT, the presented dose is the peak point dose for normal brain. The method to estimate this dose was described in detail previously in references [4] and [10]. In SRS, the presented dose is marginal X-ray or gamma-ray dose. *NA* not available

[d] Months between termination of last radiotherapy and onset of symptoms caused by radiation necrosis

[e] Amounts of betamethasone (mg/day) just prior to the treatment and 1 month after the initiation of the treatment

[f] Head and neck cancer, RN occurred in the brain parenchyma

[g] S/O pseudoprogression

Sal. Duc. Ca. salivary ductal carcinoma, *GB* glioblastoma, *Ade. Ca.* adenocarcinoma, *MM* malignant meningioma, *LC* lung cancer, *small* small cell carcinoma

[h] Bevacizumab-treated

[i] Intracerebral hemorrhage on magnetic resonance imaging (MRI)

Results

Histological analysis with H&E staining

Two representative cases of surgically excised necrotic tissue are presented in Fig. 1 (cases 9, 13). Among the 18 surgically treated cases, these 2 cases were selected for presentation because their original tumor histologies and/or treatment radiation modalities differed as shown in Table 1 and because they were expected to reveal common and universal findings in human RN. Typical pathological changes were observed with H&E staining at the border zone between the completely necrotic areas and the normal brain areas, which we term the "perinecrotic" area. The most characteristic vasculature had an enlarged lumen composed of a thin wall with a single layer of endothelial cells that mimics capillaries; this condition is described as telangiectasis. In addition, other typical pathological changes, such as microscopic bleeding, were frequently observed (Fig. 1a). In some specimens, proliferation of arterioles was also observed (data not shown). Characteristic telangiectasis was observed in all of the surgically excised necrotic tissues, irrespective of the original tumor histological type and radiation modality, as listed in Table 1 (cases 1–18). Furthermore, hyalinization or fibrinoid necrosis of the vessels was commonly found in the perinecrotic area (data not shown).

Immunohistological analysis with anti-VEGF antibody

In immunohistological analysis using anti-VEGF antibody (Figs. 2, 3), almost all astrocytes in the perinecrotic area were strongly positive for VEGF expression. This was confirmed by double staining of anti-VEGF and anti-GFAP antibody (Fig. S1). Interestingly, there was little or no expression of VEGF in the necrotic core or in the undamaged brain tissue around the necrosis (Fig. 2). These VEGF-positive astrocytes were identified as reactive astrocytes morphologically and immunohistologically, as above. They were localized only within a few millimeters from each necrotic core. Outside of this very narrow marginal zone, the number of VEGF-expressing cells decreased dramatically in all specimens. A representative VEGF expression pattern is depicted in Fig. 3. Typical angiogenesis, namely telangiectasis, was observed in the perinecrotic area where abundant expression of VEGF was concomitantly observed (Fig. 3). In the other six samples from different patients who had undergone immunohistological analyses, the same features were found with regard to VEGF expression as described above (data not shown).

Another characteristic finding was endothelial proliferation, which is composed of stratified and swollen endothelial cells and typically recognized in GB prior to radiotherapy. In our series, this endothelial proliferation was observed in RN in GB as well as in RN in malignant

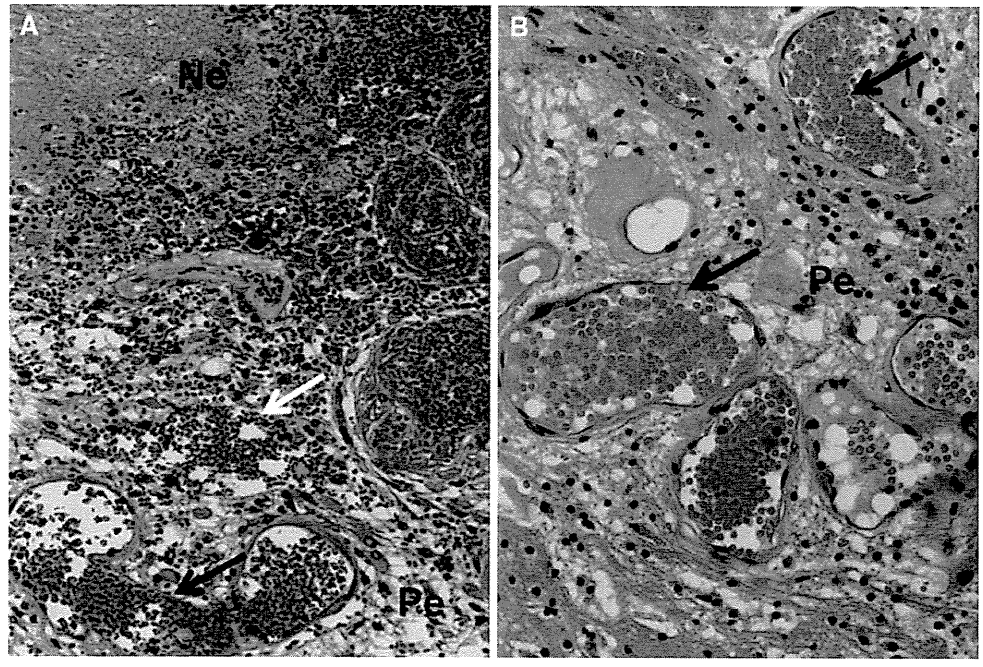

Fig. 1 Typical H&E staining of the surgical specimens from cases 9 and 13. **a** Case 13, RN derived from GB caused by XRT and BNCT. **b** Case 9, RN derived from metastatic brain tumor caused by SRS. In **a** and **b**, *black arrows* indicate telangiectasis and a *white arrow* shows bleeding in the interstitial space. *Ne* necrotic center, *Pe* perinecrotic area. In **a** and **b**, original objective magnification ×20 and ×40, respectively

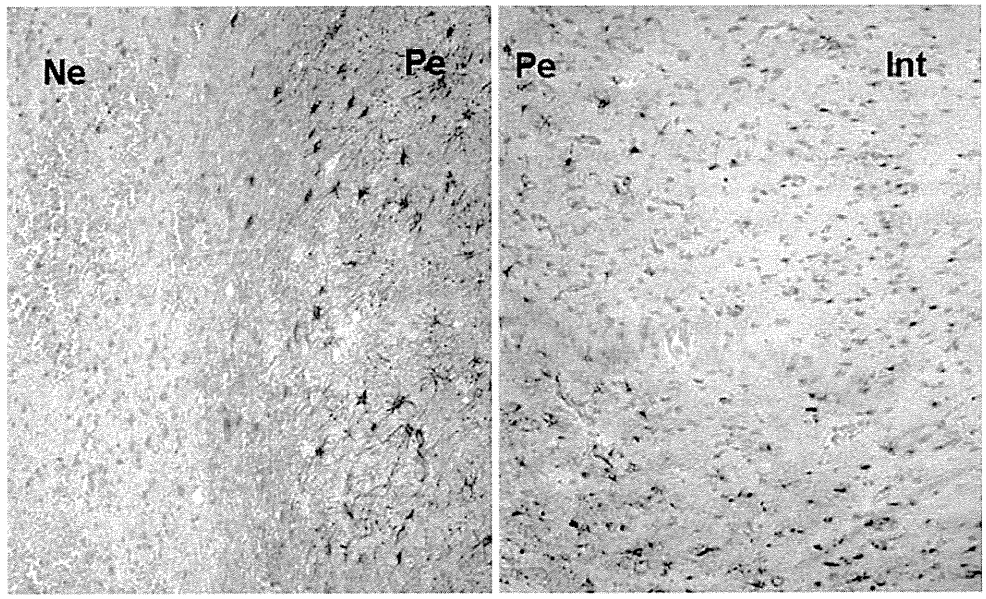

Fig. 2 Immunohistochemistry for VEGF of the surgical specimen from case 13. Many astrocyte-like cells in the perinecrotic area were strongly positive for VEGF expression. On the other hand, little or no immunoreactivity of VEGF was observed in the necrotic center or intact brain area. *Ne* necrotic center, *Pe* perinecrotic area, *Int* intact brain. Original objective magnification ×20

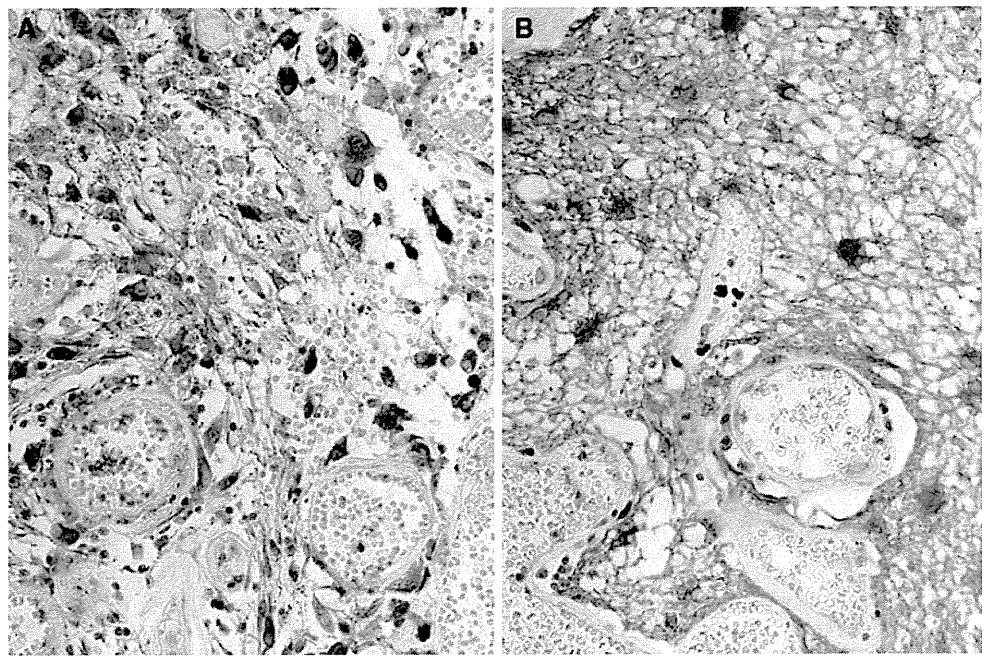

Fig. 3 Immunohistochemistry for VEGF of the perinecrotic area from cases 9 and 13. **a** and **b** are the same specimens depicted in Fig. 1. Strong immunoreactivity for VEGF and angiogenesis was observed in the perinecrotic area in **a** and **b**. Original objective magnification ×40

meningioma (data not shown), and even in the RN of the brain associated with radiotherapy for head and neck malignancies (cases 1 and 17, data not shown). It is noteworthy that the cells in endothelial proliferation and the endothelial cells in wall telangiectasis showed weaker intensity of immunoreactivity for VEGF and fewer cells, in comparison with the VEGF-positive astrocytes in the perinecrotic area (data not shown). Endothelial proliferation in the perinecrotic area was surrounded by a lot of VEGF-positive reactive astrocytes with no evidence of obvious tumor cell proliferation. It is difficult to deny completely that these endothelial proliferations derived and survived from tumor tissue after radiotherapy, especially in GB cases. However, this endothelial proliferation was also observed even in RN in the brains of head and neck cancer patients whose brains had no tumor cells. This strongly suggested that these endothelial proliferations were stimulated by the pathological signals, including VEGF, produced in the perinecrotic area.

Immunohistological analysis with anti-HIF-1α antibody

In Fig. S2, representative HIF-1α expression is depicted from three cases (cases 13, 16, and 17). HIF-1α was

strongly expressed in the cells in the perinecrotic area. At a glance, these cells look like gemistocytic astrocytes. On the other hand, little expression was observed in undamaged brain (Fig. S2A) or in the necrotic center (Fig. S2C). This tendency of HIF-1α expression was confirmed in all five of the other surgical cases examined.

Effectiveness of surgical and medical treatments for radiation necrosis

Typical rapid shrinkage of the perilesional edema in surgical treatment cases is shown in Fig. 4. Also, all patients treated with bevacizumab showed reduced perilesional edema. One example is shown in Fig. S3. The necessary amounts of steroid were reduced in 16 out of 18 surgically treated cases (88.9%) and in 7 out of 9 medically treated cases (77.8%), for a total of 23 out of 27 cases (85.2%). The Karnofsky performance score (KPS) improved in 13 out of 27 cases (50.6%). However, 3 of the 18 surgically treated cases and 1 of the 9 medically treated cases showed deterioration in KPS (Table 1).

Discussion

Several cytokines and chemokines such as VEGF, platelet-derived growth factor, and histamine can modulate vascular permeability, but single blockade of VEGF by an anti-VEGF antibody can significantly reduce the perifocal edema associated with RN in clinical cases. This result demonstrates that VEGF is one of the major permeability factors in human RN and plays a key role in its pathophysiology.

VEGF has two important biological properties. One is a strong angiogenic peptide component [18, 19], and the other is as a vascular permeability factor [20, 21]. In clinical RN, the former function may produce telangiectasis as pathological angiogenesis, and the latter function

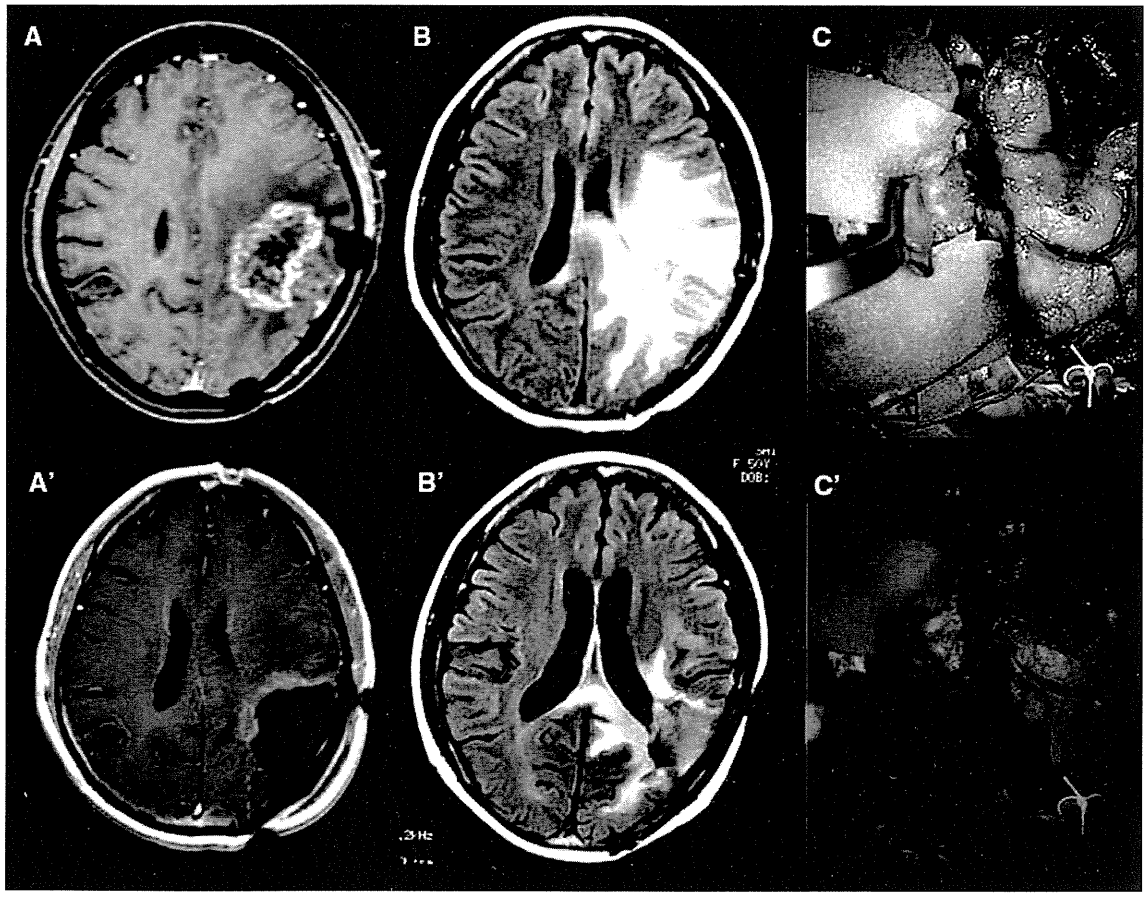

Fig. 4 Periodic changes in neuroimaging and intraoperative photographs of case 16. **a** Gd-enhanced T1 MRI just prior to excision of necrotic foci. **a′** Gd-enhanced T1 MRI 24 h after surgery. **b** FLAIR MRI just prior to excision of necrotic foci. **b′** FLAIR MRI, 1 month after surgery. Perilesional edema was decreased compared with preoperative MRI. **c** Intraoperative photograph under bright field demonstrating dissection of perinecrotic tissue from the surrounding brain. **c′** Intraoperative photograph under dark field with excitation for red fluorescence of protoporphyrin IX. *Red fluorescence* shows the perinecrotic area

may augment contrast enhancement on MRI or perilesional edema. Here, let us introduce corroboration from two previous reports that VEGF is a key molecule for inducing edema in RN. In one of those reports, overexpression of VEGF caused leaky and pathological angiogenesis in several gene therapy models [22]. In the other report, inhibition of VEGF decreased cerebral edema in rodent occlusive cerebrovascular disease models [23, 24]. In addition, results of other animal experiments directly suggested that VEGF is a key molecule in RN [25, 26].

Tissue hypoxia was found to be a potent inducer of VEGF expression in several organs, including the CNS [27]. It is known that transmission of important signals induced by hypoxia is mediated by the transcription factor HIF-1, and that strong HIF-1-mediated upregulation of VEGF occurs under hypoxia in various systems [28–30]. In our series, we demonstrated that focal hypoxia existed at the perinecrotic area, as shown in Fig. S2, by the immunohistological staining of HIF-1α. Taking these results together, we speculate that this hypoxic condition existing in contiguity with the necrotic core may trigger production of VEGF in reactive astrocytes via upregulation of HIF-1α, and that these cells seem to be the main source of VEGF in RN in the brain, as stated in "Results."

It is difficult to prove clearly that these VEGF-producing cells in RN are really reactive and nontumor astrocytes, especially in RN derived from malignant astrocytic tumors, since malignant tumor cells can also produce VEGF. However, the confluence of VEGF-producing astrocytes was similarly recognized in the perinecrotic area from malignant meningioma, metastatic brain tumor, and even in cerebral RN caused by radiotherapy for head and neck malignancies.

Endothelial cells may be another possible source of VEGF in RN [31]. Here we demonstrated that endothelial cells (not only in the wall of telangiectasis but also in endothelial proliferation) do not prominently produce VEGF in comparison with reactive astrocytes (data not shown). Therefore, we can conclude that the main VEGF source in RN in humans is its marginal gliosis consisting of concentrated reactive astrocytes, irrespective of the original tumor histology or the kinds of radiation treatment modality. This means that, when we apply surgical resection of necrotic tissue against symptomatic RN, most of the VEGF source can be efficiently removed only by several millimeters of extensive resection of the external gliosis layer in contiguity with the necrotic core. We have already reported that fluorescence of protoporphyrin IX (PpIX) derived from 5-ALA is helpful for intraoperative detection of this gliosis layer [32].

Calvo et al. [33] reported that blood vessel dilation and astrocyte hypertrophy/hyperplasia were observed in radiation injury in the brain using animal experiments, which is consistent with our observation in a study of humans. They reported that these pathological changes occurred prior to the formation of histological necrosis, although it is uncertain whether this was the case also our human study. The literature indicates that telangiectasis as well as capillary collapse occur with wall thickening and hyalinization in RN [34–37]. Telangiectasis is also reported to be a result of genesis of collateral blood flow against ischemia caused by obstruction of small venullae and arterioles, as reported in a monograph by Burger and Boyko [38]. During the early phase of RN, there is a highly characteristic fibrinoid necrosis of the small venullae and arterioles that is followed by necrosis of the surrounding brain parenchyma. This hyalinization of the vessels and fibrinoid necrosis as pathologic evidence of RN were also observed in our series (data not shown). Thus, in this early phase of RN, anticoagulants may be effective for maintaining microcirculation by preventing thrombotic obstruction in such small venullae and arterioles and consequent suppression of the secondary formation of telangiectasis following aggravation of cerebral edema. Clinically, we experience rapid shrinkage of the perilesional edema after excision of both the perinecrotic area and the necrotic center in RN. The outcomes of this intervention can be improved by intraoperative use of 5-ALA, as we reported elsewhere [32]. Red fluorescence of PpIX is considered a good detector of the gliosis layer, which consists mainly of reactive astrocytes existing in the perinecrotic tissue. Typical clinical outcomes for removal of necrotic tissue using the 5-ALA system are shown in Fig. 4.

We also demonstrated the dramatic ability of bevacizumab to decrease perilesional edema in our RN cases, as shown in Fig. S3. As Table 1 shows, both surgical removal of the necrotic foci and treatment with bevacizumab each improved the majority of cases, with improvements in performance status and decrease in required steroid dose. As we described in case 16, radiation necrosis may recur after a transient improvement by a surgical procedure. Also, we recently reported that RN recurred in some cases even after improvement by bevacizumab treatment [13]. All recurrent cases of RN, whether after surgical or bevacizumab treatment, responded well to rechallenge by bevacizumab.

In conclusion, the findings described in this manuscript suggest that VEGF-producing astrocytes concentrated in the perinecrotic area might be a universal cause of pathological angiogenesis and the subsequent perilesional edema typically found in RN of the brain, irrespective of the applied radiation modality, the irradiated tumor histology, and whether or not the tumor exists in the brain. Medical treatment with anti-VEGF antibody, bevacizumab or surgical resection of necrotic tissue may serve to decrease this edema and provide immediate

symptomatic improvements stemming from efficient reduction of VEGF in the brain.

Acknowledgments The first two authors contributed equally to this work. This work was partly supported by Grants-in-Aid for Scientific Research (B) (16390422 and 19390385) from the Japanese Ministry of Education, Culture, Sports, Science, and Technology to S.-I.M. This work was also supported in part by the Takeda Science Foundation for Osaka Medical College and in part by a grant from the OMC Science Frontier Program for the Promotion of Research in Osaka Medical College to S.-I.M. We appreciate the help of Dr. Shingo Takano, Department of Neurosurgery, Tsukuba University, for providing information on immunohistochemistry of hypoxia-inducible factor-1α; and the help of Hiroko Kuwabara, Department of Pathology, Osaka Medical College, for fruitful discussion on the histological findings of the pathological specimens.

Conflict of interest The authors declare no conflict of interest.

References

1. Hopewell JW (1998) Radiation injury to the central nervous system. Med Pediatr Oncol Suppl 1:1–9
2. Fitzek MM, Thornton AF, Rabinov JD, Lev MH, Pardo FS, Munzenrider JE, Okunieff P, Bussiere M, Braun I, Hochberg FH, Hedley-Whyte ET, Liebsch NJ, Harsh GRt (1999) Accelerated fractionated proton/photon irradiation to 90 cobalt gray equivalent for glioblastoma multiforme: results of a phase II prospective trial. J Neurosurg 91:251–260
3. Iuchi T, Hatano K, Narita Y, Kodama T, Yamaki T, Osato K (2006) Hypofractionated high-dose irradiation for the treatment of malignant astrocytomas using simultaneous integrated boost technique by IMRT. Int J Radiat Oncol Biol Phys 64:1317–1324
4. Kawabata S, Miyatake S, Kuroiwa T, Yokoyama K, Doi A, Iida K, Miyata S, Nonoguchi N, Michiue H, Takahashi M, Inomata T, Imahori Y, Kirihata M, Sakurai Y, Maruhashi A, Kumada H, Ono K (2009) Boron neutron capture therapy for newly diagnosed glioblastoma. J Radiat Res 50:51–60
5. Miyatake S, Kawabata S, Kajimoto Y, Aoki A, Yokoyama K, Yamada M, Kuroiwa T, Tsuji M, Imahori Y, Kirihata M, Sakurai Y, Masunaga S, Nagata K, Maruhashi A, Ono K (2005) Modified boron neutron capture therapy for malignant gliomas performed using epithermal neutron and two boron compounds with different accumulation mechanisms: an efficacy study based on findings on neuroimages. J Neurosurg 103:1000–1009
6. Tanaka M, Ino Y, Nakagawa K, Tago M, Todo T (2005) High-dose conformal radiotherapy for supratentorial malignant glioma: a historical comparison. Lancet Oncol 6:953–960
7. Ohguri T, Imada H, Kohshi K, Kakeda S, Ohnari N, Morioka T, Nakano K, Konda N, Korogi Y (2007) Effect of prophylactic hyperbaric oxygen treatment for radiation-induced brain injury after stereotactic radiosurgery of brain metastases. Int J Radiat Oncol Biol Phys 67:248–255
8. Guttin PH (1991) Treatment of radiation necrosis of the brain. Raven, New York
9. Leibel SA, Gutin PH, Wara WM, Silver PS, Larson DA, Edwards MS, Lamb SA, Ham B, Weaver KA, Barnett C et al (1989) Survival and quality of life after interstitial implantation of removable high-activity iodine-125 sources for the treatment of patients with recurrent malignant gliomas. Int J Radiat Oncol Biol Phys 17:1129–1139
10. Levin VA, Bidaut L, Hou P, Kumar AJ, Wefel JS, Bekele BN, Prabhu S, Loghin M, Gilbert MR, Jackson EF (2011) Randomized double-blind placebo-controlled trial of bevacizumab therapy for radiation necrosis of the central nervous system. Int J Radiat Oncol Biol Phys 79(5):1487–1495
11. Gonzalez J, Kumar AJ, Conrad CA, Levin VA (2007) Effect of bevacizumab on radiation necrosis of the brain. Int J Radiat Oncol Biol Phys 67:323–326
12. Torcuator R, Zuniga R, Mohan YS, Rock J, Doyle T, Anderson J, Gutierrez J, Ryu S, Jain R, Rosenblum M, Mikkelsen T (2009) Initial experience with bevacizumab treatment for biopsy confirmed cerebral radiation necrosis. J Neurooncol 94:63–68
13. Furuse M, Kawabata S, Kuroiwa T, Miyatake SI (2010) Repeated treatments with bevacizumab for recurrent radiation necrosis in patients with malignant brain tumors: a report of 2 cases. J Neurooncol 102(3):471–475
14. Miyatake S, Kawabata S, Nonoguchi N, Yokoyama K, Kuroiwa T, Matsui H, Ono K (2009) Pseudoprogression in boron neutron capture therapy for malignant gliomas and meningiomas. Neuro Oncol 11:430–436
15. Miyashita M, Miyatake S, Imahori Y, Yokoyama K, Kawabata S, Kajimoto Y, Shibata MA, Otsuki Y, Kirihata M, Ono K, Kuroiwa T (2008) Evaluation of fluoride-labeled boronophenylalanine-PET imaging for the study of radiation effects in patients with glioblastomas. J Neurooncol 89:239–246
16. Stummer W, Novotny A, Stepp H, Goetz C, Bise K, Reulen HJ (2000) Fluorescence-guided resection of glioblastoma multiforme by using 5-aminolevulinic acid-induced porphyrins: a prospective study in 52 consecutive patients. J Neurosurg 93:1003–1013
17. Stummer W, Stocker S, Wagner S, Stepp H, Fritsch C, Goetz C, Goetz AE, Kiefmann R, Reulen HJ (1998) Intraoperative detection of malignant gliomas by 5-aminolevulinic acid-induced porphyrin fluorescence. Neurosurgery 42:518–525 discussion 525–516
18. Keck PJ, Hauser SD, Krivi G, Sanzo K, Warren T, Feder J, Connolly DT (1989) Vascular permeability factor, an endothelial cell mitogen related to PDGF. Science 246:1309–1312
19. Leung DW, Cachianes G, Kuang WJ, Goeddel DV, Ferrara N (1989) Vascular endothelial growth factor is a secreted angiogenic mitogen. Science 246:1306–1309
20. Connolly DT, Heuvelman DM, Nelson R, Olander JV, Eppley BL, Delfino JJ, Siegel NR, Leimgruber RM, Feder J (1989) Tumor vascular permeability factor stimulates endothelial cell growth and angiogenesis. J Clin Invest 84:1470–1478
21. Connolly DT, Olander JV, Heuvelman D, Nelson R, Monsell R, Siegel N, Haymore BL, Leimgruber R, Feder J (1989) Human vascular permeability factor. Isolation from U937 cells. J Biol Chem 264:20017–20024
22. Zacchigna S, Tasciotti E, Kusmic C, Arsic N, Sorace O, Marini C, Marzullo P, Pardini S, Petroni D, Pattarini L, Moimas S, Giacca M, Sambuceti G (2007) In vivo imaging shows abnormal function of vascular endothelial growth factor-induced vasculature. Hum Gene Ther 18:515–524
23. Kimura R, Nakase H, Tamaki R, Sakaki T (2005) Vascular endothelial growth factor antagonist reduces brain edema formation and venous infarction. Stroke 36:1259–1263
24. van Bruggen N, Thibodeaux H, Palmer JT, Lee WP, Fu L, Cairns B, Tumas D, Gerlai R, Williams SP, van Lookeren Campagne M, Ferrara N (1999) VEGF antagonism reduces edema formation and tissue damage after ischemia/reperfusion injury in the mouse brain. J Clin Invest 104:1613–1620
25. Li YQ, Ballinger JR, Nordal RA, Su ZF, Wong CS (2001) Hypoxia in radiation-induced blood-spinal cord barrier breakdown. Cancer Res 61:3348–3354
26. Nordal RA, Nagy A, Pintilie M, Wong CS (2004) Hypoxia and hypoxia-inducible factor-1α target genes in central nervous

system radiation injury: a role for vascular endothelial growth factor. Clin Cancer Res 10:3342–3353
27. Minchenko A, Bauer T, Salceda S, Caro J (1994) Hypoxic stimulation of vascular endothelial growth factor expression in vitro and in vivo. Lab Invest 71:374–379
28. Fang J, Yan L, Shing Y, Moses MA (2001) HIF-1alpha-mediated up-regulation of vascular endothelial growth factor, independent of basic fibroblast growth factor, is important in the switch to the angiogenic phenotype during early tumorigenesis. Cancer Res 61:5731–5735
29. Ikeda E, Achen MG, Breier G, Risau W (1995) Hypoxia-induced transcriptional activation and increased mRNA stability of vascular endothelial growth factor in C6 glioma cells. J Biol Chem 270:19761–19766
30. Shweiki D, Itin A, Soffer D, Keshet E (1992) Vascular endothelial growth factor induced by hypoxia may mediate hypoxia-initiated angiogenesis. Nature 359:843–845
31. Kalaria RN, Cohen DL, Premkumar DR, Nag S, LaManna JC, Lust WD (1998) Vascular endothelial growth factor in Alzheimer's disease and experimental cerebral ischemia. Brain Res Mol Brain Res 62:101–105
32. Miyatake S, Kuroiwa T, Kajimoto Y, Miyashita M, Tanaka H, Tsuji M (2007) Fluorescence of non-neoplastic, magnetic resonance imaging-enhancing tissue by 5-aminolevulinic acid: case report. Neurosurgery 61:E1101–E1103 discussion E1103–1104
33. Calvo W, Hopewell JW, Reinhold HS, Yeung TK (1988) Time- and dose-related changes in the white matter of the rat brain after single doses of X rays. Br J Radiol 61:1043–1052
34. Burger PC, Mahley MS Jr, Dudka L, Vogel FS (1979) The morphologic effects of radiation administered therapeutically for intracranial gliomas: a postmortem study of 25 cases. Cancer 44:1256–1272
35. Gaensler EH, Dillon WP, Edwards MS, Larson DA, Rosenau W, Wilson CB (1994) Radiation-induced telangiectasia in the brain simulates cryptic vascular malformations at MR imaging. Radiology 193:629–636
36. Poussaint TY, Siffert J, Barnes PD, Pomeroy SL, Goumnerova LC, Anthony DC, Sallan SE, Tarbell NJ (1995) Hemorrhagic vasculopathy after treatment of central nervous system neoplasia in childhood: diagnosis and follow-up. AJNR Am J Neuroradiol 16:693–699
37. Rabin BM, Meyer JR, Berlin JW, Marymount MH, Palka PS, Russell EJ (1996) Radiation-induced changes in the central nervous system and head and neck. Radiographics 16:1055–1072
38. Burger P, Boyko O (1991) The pathology of central nervous system radiation injury. In: Gutin PH, Leibel SA, Sheline GE (eds) Radiation injury to the nervous system. Raven Press, New York, pp 191–208

Applied Radiation and Isotopes 69 (2011) 1796–1799

Contents lists available at ScienceDirect

Applied Radiation and Isotopes

journal homepage: www.elsevier.com/locate/apradiso

Phase II clinical study of boron neutron capture therapy combined with X-ray radiotherapy/temozolomide in patients with newly diagnosed glioblastoma multiforme—Study design and current status report

Shinji Kawabata [a,*], Shin-Ichi Miyatake [a], Ryo Hiramatsu [a], Yuki Hirota [a], Shiro Miyata [a], Yoko Takekita [a], Toshihiko Kuroiwa [a], Mitsunori Kirihata [b], Yoshinori Sakurai [c], Akira Maruhashi [c], Koji Ono [c]

[a] Department of Neurosurgery, Osaka Medical College, 2-7 Daigaku-Machi, Takatsuki, Osaka 569-8686, Japan
[b] Graduate School of Life and Environmental Sciences, Osaka Prefecture University, 1-1 Gakuen-cho, Naka-ku, Sakai, Osaka 599-8931, Japan
[c] Kyoto University Research Reactor Institute, 2 Asashiro-Nishi, Kumatori-cho, Sennan-gun, Osaka 590-0494, Japan

ARTICLE INFO

Available online 21 March 2011

Keywords:
Boron neutron capture therapy
Fractionated X-ray irradiation
Glioblastoma
Temozolomide
Phase II clinical study

ABSTRACT

Recently, we reported our clinical experiences of boron neutron capture therapy (BNCT) for the newly diagnosed glioblastoma. The major differences of our protocol from the other past studies were simultaneous use of both sodium borocapate and boronophenylalanine, and combination with fractionated X-ray irradiation.

These results showed the efficacy of combination therapy with external beam X-ray irradiation and BNCT. For our future study, we planned the multi-centric phase II clinical study for newly diagnosed glioblastoma patients in Japan (OSAKA-TRIBRAIN0902, NCT00974987).

1. Introduction

Recently, we analyzed and reported our clinical experiences of boron neutron capture therapy (BNCT) for the newly diagnosed malignant glioma patients (Kawabata et al., 2009). These results showed the efficacy of combination therapy with external beam X-ray irradiation and BNCT. Based on this study, we planned the multi-centric phase II clinical study, named "*Boron Neutron Capture Therapy, Radiation Therapy, and Temozolomide in Treating Patients with Newly Diagnosed Glioblastoma Multiforme*" (OSAKA-TRIBRAIN0902, NCT00974987).

2. Methods/design

Prior to design of new version of the protocol for multi-centric study, we analyzed our previous clinical results of all the patients with malignant glioma treated by BNCT. Main part of the retrospective analysis was as follows: 1 overall survival, 2 efficacy of additional fractionated X-ray irradiation, 3 administration of the boron compounds, and 4 toxicity. This project was approved by the Ethical Committee of Osaka Medical College and by the BNCT Committee of Kyoto University Research Reactor Institute, Japan Atomic Energy Agency. Individual cases were discussed and selected by the latter committee and the signing of the informed consent by each patient. Based on this retrospective analysis, the multi-centric phase II clinical study was planned.

3. Result

3.1. Retrospective analysis of our previous clinical studies

3.1.1. Overall survival

Patients treated with BNCT ($n=21$) had a median survival time (MST) of 15.6 months (95% confidence interval (CI): 12.2–23.9) after diagnosis. This was significantly longer than the MST for the historical controls at our institute who were treated with surgical removal followed by XRT and chemotherapy ($n=27$, MST was 10.3 months (95% CI: 7.4–13.2, log-rank test $p=0.004$, Hazard ratio (HR)=0.40).

3.1.2. Efficacy of additional fractionated X-ray irradiation

The MST of the patients treated with BNCT followed by XRT boost was 23.5 months (95% CI: 10. 2—undetermined, HR (vs. control)=0.32) after diagnosis ($n=11$), and that of the patients treated with BNCT only ($n=10$) was 14.1 months (95% CI: 9.9–18.5), although the difference was not statistically significant among these two groups.

* Corresponding author. Tel.: +81 72 683 1221; fax: +81 72 681 1674.
E-mail address: neu046@poh.osaka-med.ac.jp (S. Kawabata).

0969-8043/$ - see front matter © 2011 Elsevier Ltd. All rights reserved.
doi:10.1016/j.apradiso.2011.03.014

3.1.3. Administration of the boron compounds

In our previous study for all the patients with malignant brain tumor included several doses of boron compounds especially for BPA, 250, 500, 700 mg/kg body weight. Blood boron concentration was increased by escalation of the BPA dose. The continuous infusion with reduced BPA dose during irradiation (400 mg/kg for 2 h+100 mg/kg for 1 h, previously used for head and neck cancer in KURRI) was also used and this was useful for dose estimation of BNCT because the blood boron concentration similar as 700 mg BPA/kg was kept during irradiation whereas a decline of the blood level was remarkable when we terminated BPA just before neutron irradiation.

3.1.4. Toxicity

Adverse events were assessed by common terminology criteria for adverse events (CTCAE) v3.0. Grade 3/4 blood/bone marrow toxicity (hemoglobin, leukocytes, neutrophils, and platelets) were 11% in 250 mg/kg, 17% in 500 mg/kg, and 28% in 700 mg/kg. Other Grade 3/4 adverse events (seizure, AST, ALT, amylase, creatinine) were 64% in 250 mg/kg, 25% in 500 mg/kg, and 63% in 700 mg/kg. All of these adverse events were reversible and transient. Radiation induced edema and/or necrosis occurred mainly in the area that was available for high-dose irradiation by BNCT nearly the surface of the brain of the patients treated with BNCT+XRT.

3.2. Newly designed protocol for multi-centric study

The major differences of our newly planned protocol from the other past BNCT studies were simultaneous use of both sodium borocapate (BSH) and boronophenylalanine (BPA) (Kawabata et al., 2003; Miyatake et al., 2005, 2009b), and combination with X-ray irradiation (XRT) (Fig. 1) (Kawabata et al., 2009). In our single institution experience, this protocol was significantly beneficial for extent of survival of the patients with newly diagnosed glioblastoma (GB).

3.2.1. Protocol objectives

A phase II, multi-center, study for newly diagnosed GBs using BNCT, additional 24 Gy XRT with 3 gradient and concomitant and adjuvant chemotherapy with temozolomide (TMZ) (Fig. 2) is conducted to evaluate overall survival as primary endpoint and tumor response and adverse effects as secondary endpoints.

3.2.2. Outline

Protocol treatments consist of BNCT, additional 24 Gy XRT and chemotherapy with TMZ. Prescription dose by BNCT is regulated as not to be more than 13 Gy-Eq for normal brain. Additional XRT is given with 3 gradient such as 8, 16, and 24 Gy from the surface of scalp to the bottom of tumor infiltrated zone (Fig. 3). Chemotherapy with TMZ is applied concomitantly during XRT treatments and adjuvant chemotherapy with the same agent is repeated in outpatient clinic (Stupp et al., 2005).

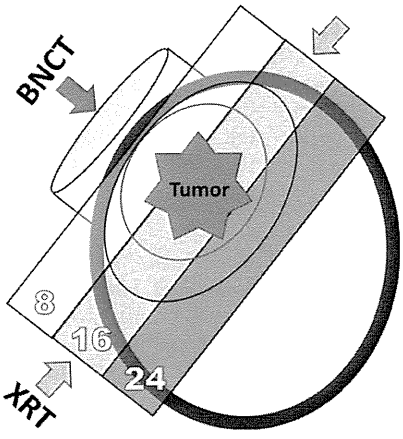

Fig. 1. This is an image illustration of the protocol combined with BNCT and 3 gradient fractionated XRT. The details refer to the methods/design section.

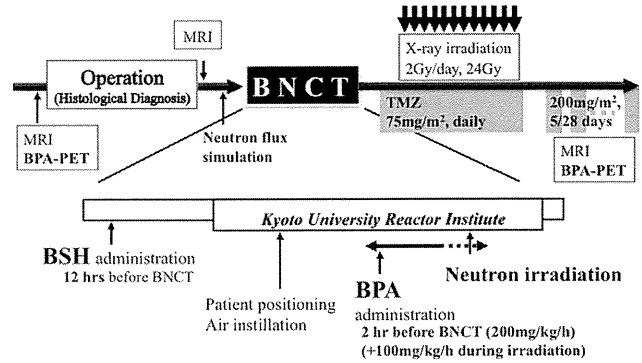

Fig. 2. This figure shows a flow of overall treatment, using boron neutron capture therapy(BNCT), additional 24 Gy X-ray irradiation (XRT) with 3 gradient and concomitant and adjuvant chemotherapy with temozolomide (TMZ). The most important point in our protocol is diagnosis and treatment of radiation effects using ^{18}F-BPA-PET study during follow-up, not only for dose planning.

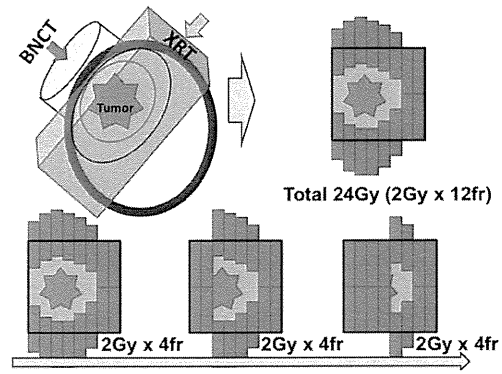

Fig. 3. This figure shows a method of XRT, additional 24 Gy (2 Gy daily × 12 fractions) XRT with 3 gradient, concretely.

3.2.3. Protocol entry criteria/disease characteristics

Newly diagnosed GB patients whose histology is confirmed by surgery are included in the study.

3.2.4. Patient characteristics/inclusion criteria

Histopathology: newly diagnosed GB, age range: over 15 and up to 75 years, Karnofsky performance status: more than 60%.

All inclusion criteria for the study:

(1) Patients with definitive newly diagnosed GB by histopathology. (2) The tumor locates at a supra-tentorial hemisphere. (3) The deepest part of the tumor should be less than 6 cm from the scalp. Even if the bottom of the tumor is more than 6 cm from the scalp, the patients may be included in the study, if the air instillation into tumor-removed cavity is possible (Kawabata et al., 2009; Miyatake et al., 2009b; Sakurai et al., 2006). (4) Life expectancy is more than 3 months. (5) Patients who demonstrate appropriate bone marrow, hepatic, and renal functions in laboratory tests within four weeks before the registration. (a) Leukocyte count $\geq 3000/\mu L$, (b) Hemoglobin level ≥ 8.0 g/dL, (c) Platelet

count $\geq 10.0 \times 10^4/\mu L$, (d) Serum creatine level ≤ 1.5 mg/dL, (e) ALT levels ≤ 100 IU/L, and (f) AST levels ≤ 100 IU/L. (6) Patients who agreed to participate in this study.

All exclusion criteria for the study:

(1) Patients who have been treated with chemotherapy or radiotherapy. (2) Female patients in definitive or possible pregnancy or in breast-feeding. (3) Patients with phenylketonuria. (4) Patients with grade III or IV in New York Heart Association (NYHA) classification. (5) Patients with cerebrospinal fluid (CSF) dissemination. (6) Other patients whose participation in the present study is considered inappropriate by a Principal Investigator or Clinical Investigator.

3.2.5. Projected accrual

Target number of subjects was settled as 45 cases. The total number of the patients required in this study is estimated based on our previous BNCT results (Kawabata et al., 2009) and analyzed by Shoenfeld & Richter method with a significant level of 0.05, a power of 80%, registration period of 2 years and follow up period of 2 years, 2.5 months therapy gain by TMZ use. Because about 10% of patients would not be evaluated, the sample size was set at 45 cases.

3.2.6. Statistical section

Outcome (Primary Outcome: overall survival; Secondary Outcome: (1) tumor response and (2) adverse effects)

4. Discussions

Glioblastoma (GB) is currently not curable and the prognosis of it is very poor. A world-wide standard care of newly diagnosed GB is postoperative XRT with concomitant and adjuvant chemotherapy with new alkylating agent TMZ. This standard treatment for newly diagnosed GB prolonged the median survival time (MST) of patients from 12.1 to 14.6 months in comparison with XRT alone, which is still pessimistic clinical result of this disease. Therefore an alternative promising treatment should be developed for the improvement of the prognosis of newly diagnosed GB.

On the other hand, boron neutron capture therapy (BNCT) is tumor-selective particle radiation. Tumor-seeking boron compounds boronophenylalanine (BPA) and sodium borocapate (BSH) can be delivered selectively in GB tissue with high contrast of accumulation in comparison with normal brain tissue. This tumor selective accumulation of boron compounds is followed by neutron irradiation, which produced high linear energy transfer particles (alpha particle and re-coiled Li nucleus). Thereafter these particles can destroy tumor cells selectively with high efficiency (Barth et al., 2005). The principal investigator of this clinical trial published the excellent survival data of 21 cases of newly diagnosed GB treated by BNCT with the MST of 15.6 months without TMZ. Moreover additional 20–30 Gy XRT prolonged the MST up to 23.5 months in 11 cases without TMZ (Kawabata et al., 2009). These strategies were also confirmed by pre-clinical bench works (Barth et al., 2004). These are the background of this clinical trial. Thereafter in this trial, the protocol is composed of BNCT, followed by 24 Gy XRT with concomitant and adjuvant chemotherapy with TMZ for newly diagnosed GB patients.

Based on our former BNCT clinical experience, we included the following points in a new protocol. Use the two boron compounds, BSH and BPA, in combination (Ono et al., 1999; Yokoyama et al., 2006). The schedule of the administration of boron compounds is settled as follows: 13 h before the neutron irradiation, 100 mg/kg of BSH will be intravenously infused for 1 h, and 500 mg/kg of BPA will be infused continuously 200 mg/kg/h for 2 h before the irradiation and reduced for 100 mg/kg/h during irradiation to the patients. During continuous BPA infusion of reduced dose as 100 mg/kg, neutrons irradiation is performed. Limiting factor for the irradiation time is settled for the normal brain dose as 13 Gy-Eq. Based on our previous clinical study (Kawabata et al., 2009), the Hazard ratio of BNCT vs. XRT was simulated as 0.4; so the total estimated number of the patients who should be included in our new study became 45 totally. Primary endpoint is overall survival and these patients will be followed up for 2 years after the last patient treatment. The most important point in our protocol is diagnosis and treatment of radiation effects such as swelling, radiation induced edema, transient expansion of the tumor, pseudo-progression/response, and radiation necrosis. ^{18}F-BPA-PET study is included for the diagnosis of these pathologies (Imahori et al., 1998; Miyashita et al., 2008; Miyatake et al., 2009a).

Seven Japanese neurosurgical institutions were already entered for this study (September, 2010). These institute does not have ongoing other clinical trials for newly diagnosed GB. The protocol was approved for each IRB in all of these. Also in these 6 institutes, we retrospectively reviewed all of the patients with same inclusion criteria (as same as TRIBRAIN0902) treated by conventional XRT/TMZ+TMZ therapy (Stupp et al., 2005). These patients will be followed up for 2 years and will be compared with our phase II clinical data (BNCT+XRT/TMZ+TMZ).

Acknowledgments

This project was supported by the grant-in-aid for Scientific Research from the Ministry of Health, Labor and Welfare of Japan to S-I. Miyatake. This work was also partly supported by Scientific Research from the Japanese Ministry of Education, Science, and Culture to S. Miyata (Start-up for young researcher, 21890283), S. Kawabata (Scientific Research C, 20591728), and Y. Takekita (Grant-in-Aid for Young Scientist B, 22791361). This work was also supported in part by the Takeda Science Foundation for S. Kawabata.

References

Barth, R.F., Coderre, J.A., Vicente, M.G., Blue, T.E., 2005. Boron neutron capture therapy of cancer: current status and future prospects. Clin. Cancer Res. 11, 3987–4002.

Barth, R.F., Grecula, J.C., Yang, W., Rotaru, J.H., Nawrocky, M., Gupta, N., Albertson, B.J., Ferketich, A.K., Moeschberger, M.L., Coderre, J.A., Rofstad, E.K., 2004. Combination of boron neutron capture therapy and external beam radiotherapy for brain tumors. International J. Radiat. Oncol. Biol. Phys. 58, 267–277.

Imahori, Y., Ueda, S., Ohmori, Y., Sakae, K., Kusuki, T., Kobayashi, T., Takagaki, M., Ono, K., Ido, T., Fujii, R., 1998. Positron emission tomography-based boron neutron capture therapy using boronophenylalanine for high-grade gliomas: part I and II. Clin. Cancer Res. 4, 1825–1841.

Kawabata, S., Miyatake, S., Kajimoto, Y., Kuroda, Y., Kuroiwa, T., Imahori, Y., Kirihata, M., Sakurai, Y., Kobayashi, T., Ono, K., 2003. The early successful treatment of glioblastoma patients with modified boron neutron capture therapy. Report of two cases. J. Neuro-Oncology 65, 159–165.

Kawabata, S., Miyatake, S., Nonoguchi, N., Hiramatsu, R., Iida, K., Miyata, S., Yokoyama, K., Doi, A., Kuroda, Y., Kuroiwa, T., Michiue, H., Kumada, H., Kirihata, M., Imahori, Y., Maruhashi, A., Sakurai, Y., Suzuki, M., Masunaga, S., Ono, K., 2009. Survival benefit from boron neutron capture therapy for the newly diagnosed glioblastoma patients. Appl. Radiat. Isot. 67, S15–S18.

Miyashita, M., Miyatake, S., Imahori, Y., Yokoyama, K., Kawabata, S., Kajimoto, Y., Shibata, M.A., Otsuki, Y., Kirihata, M., Ono, K., Kuroiwa, T., 2008. Evaluation of fluoride-labeled boronophenylalanine-PET imaging for the study of radiation effects in patients with glioblastomas. J. Neuro-Oncology 89, 239–246.

Miyatake, S., Kawabata, S., Kajimoto, Y., Aoki, A., Yokoyama, K., Yamada, M., Kuroiwa, T., Tsuji, M., Imahori, Y., Kirihata, M., Sakurai, Y., Masunaga, S., Nagata, K., Maruhashi, A., Ono, K., 2005. Modified boron neutron capture therapy for malignant gliomas performed using epithermal neutron and two boron compounds with different accumulation mechanisms: an efficacy study based on findings on neuroimages. J. Neurosurg. 103, 1000–1009.

Miyatake, S., Kawabata, S., Nonoguchi, N., Yokoyama, K., Kuroiwa, T., Matsui, H., Ono, K., 2009a. Pseudoprogression in boron neutron capture therapy for malignant gliomas and meningiomas. Neuro-Oncology 11, 430–436.

Miyatake, S., Kawabata, S., Yokoyama, K., Kuroiwa, T., Michiue, H., Sakurai, Y., Kumada, H., Suzuki, M., Maruhashi, A., Kirihata, M., Onoc, K., 2009b. Survival benefit of boron neutron capture therapy for recurrent malignant gliomas. Appl. Radiat. Isot. 67, S22–S24.

Ono, K., Masunaga, S., Suzuki, M., Kinashi, Y., Takagaki, M., Akaboshi, M., 1999. The combined effect of boronophenylalanine and borocaptate in boron neutron capture therapy for SCCVII tumors in mice. Int. J. Radiat. Oncol. Biol. Phys. 43, 431–436.

Sakurai, Y., Ono, K., Miyatake, S., Maruhashi, A., 2006. Improvement effect on the depth-dose distribution by CSF drainage and air infusion of a tumour-removed cavity in boron neutron capture therapy for malignant brain tumours. Phys. Med. Biol. 51, 1173–1183.

Stupp, R., Mason, W.P., van den Bent, M.J., Weller, M., Fisher, B., Taphoorn, M.J., Belanger, K., Brandes, A.A., Marosi, C., Bogdahn, U., Curschmann, J., Janzer, R.C., Ludwin, S.K., Gorlia, T., Allgeier, A., Lacombe, D., Cairncross, J.G., Eisenhauer, E., Mirimanoff, R.O., 2005. Radiotherapy plus concomitant and adjuvant temozolomide for glioblastoma. N. Engl. J. Med. 352, 987–996.

Yokoyama, K., Miyatake, S., Kajimoto, Y., Kawabata, S., Doi, A., Yoshida, T., Asano, T., Kirihata, M., Ono, K., Kuroiwa, T., 2006. Pharmacokinetic study of BSH and BPA in simultaneous use for BNCT. J. Neuro-Oncology 78, 227–232.

Neuro-Oncology 13(11):1234–1243, 2011.
doi:10.1093/neuonc/nor116
Advance Access publication August 8, 2011

NEURO-ONCOLOGY

Enhanced expression of coproporphyrinogen oxidase in malignant brain tumors: CPOX expression and 5-ALA–induced fluorescence

Kenkichi Takahashi, Naokado Ikeda, Naosuke Nonoguchi, Yoshinaga Kajimoto, Shin-Ichi Miyatake, Yuichiro Hagiya, Shun-Ichiro Ogura, Hiroshi Nakagawa, Toshihisa Ishikawa, and Toshihiko Kuroiwa

Department of Neurosurgery, Osaka Medical College, Osaka, Japan (K.T., N.I., N.N., Y.K., S.-I.M., T.K.); Graduate School of Bioscience and Biotechnology, Tokyo Institute of Technology, Yokohama, Japan (Y.H., S.-I.O., H.N., T.I.); RIKEN Omics Science Center, Yokohama, Japan (T.I.)

In photodynamic diagnosis, 5-aminolevulinic acid (5-ALA) is widely used for the fluorescence-guided resection of malignant brain tumors, where 5-ALA is converted to protoporphyrin IX, which exhibits strong fluorescence. Little is known, however, about the detailed molecular mechanisms underlying 5-ALA–induced fluorescence. To resolve this issue, we analyzed transcriptome profiles for the genes encoding enzymes, transporters, and a transcription factor involved in the porphyrin-biosynthesis pathway. By quantitative real-time (qRT)-PCR, we measured the mRNA levels of those genes in a total of 20 tumor samples that had been surgically resected from brain tumor patients at the Department of Neurosurgery of Osaka Medical College from 2008 to 2009. We selected 10 tumor samples with no 5-ALA–induced fluorescence, among which 2 were glioblastomas and 8 were metastatic brain tumors. Another 10 tumor samples were selected with strong fluorescence, among which 7 were glioblastomas and 3 were metastatic brain tumors. The qRT-PCR analysis study of these latter 10 samples revealed predominantly high levels of the mRNA of the coproporphyrinogen oxidase (CPOX) gene. The high mRNA level of CPOX expression was significantly well correlated with the phenotype of strong 5-ALA–induced fluorescence ($P = .0003$). These findings were further confirmed by immunohistochemical studies with a CPOX-specific antibody. It is concluded that induction of CPOX gene expression is one of the key molecular mechanisms underlying the 5-ALA–induced fluorescence of malignant brain tumors. The induction mechanism for the CPOX gene in brain tumors remains to be elucidated.

Keywords: coproporphyrinogen oxidase, malignant glioma, metastatic brain tumor, photodynamic diagnosis.

Received March 15, 2011; accepted June 24, 2011.

Corresponding Author: Naokado Ikeda, M.D.,Ph.D., Department of Neurosurgery, Osaka Medical College, 2–7 Daigaku-machi, Takatsuki, Osaka 569-8686, Japan (neu094@poh.osaka-med.ac.jp).

Photodynamic diagnosis (PDD) is achieved by a photon-induced physicochemical reaction such as that induced by excitation of a photosensitizer exposed to light.[1–4] In recent years, remarkable advances have been made in PDD technology that make it easier to reliably achieve complete excision of malignant gliomas[5,6] and meningiomas.[7] Nevertheless, the extent of tumor resection required in patients with glioblastoma multiforme has remained controversial.[8] Fluorescence-guided gross total resection has been established; however, and it has prolonged the survival time of glioblastoma patients.[9]

In present-day PDD technology, the porphyrin precursor 5-aminolevulinic acid (5-ALA) is widely used for the fluorescence-guided resection of malignant brain tumors. 5-ALA is a naturally occurring amino acid derivative and nonfluorescing substance that preferentially accumulates in tumor cells and is metabolized to protoporphyrin IX (PpIX) via the porphyrin-biosynthesis pathway.[10] PpIX that accumulates in intracellular compartments of tumor cells exhibits strong red fluorescence under excitation light of an appropriate wavelength.[11] PpIX-accumulating tumor cells can thus be intraoperatively visually discerned from the surrounding normal cells that accumulate PpIX to much lesser extents.[12–14] Chemonavigation based on the induction of PpIX by 5-ALA administration enables the fluorescence-guided resection of malignant brain tumors. Thus, PDD with 5-ALA supports the complete resection of contrast-enhanced tumors, leading to improved progression-free survival in patients with malignant glioma.[9]

Previous studies have demonstrated that the intensity of PpIX fluorescence was correlated with the cellular density, the MIB-1 labeling index as an indicator of proliferative activity, and the area of CD-31 staining as a measure for neovascularity[6] as well as blood-brain barrier permeability.[15] Despite all 4 factors, however, 5-ALA–induced PpIX fluorescence is not observed in certain types of tumors, especially in metastatic brain tumors.

To date, little is known about the molecular mechanisms underlying PpIX accumulation in clinical malignant brain tumors following administration of 5-ALA. We hypothesized that malignant brain tumors might exhibit distinct gene expression patterns associated with activated enzymes or transporters in the porphyrin-biosynthesis pathway and that such differences in genetic expression patterns would represent the fluorescence intensity in malignant brain tumors. In the present study, we have used quantitative real-time (qRT)-PCR to analyze the expression profiles of genes critically involved in the porphyrin-biosynthesis pathway. We found that the level of mRNA encoding coproporphyrinogen oxidase (CPOX) was remarkably increased in malignant brain tumors that exhibited strong fluorescence of PpIX after 5-ALA administration.

Materials and Methods

Collection of Tumor Samples and Surgical Operation for Brain Tumor Patients

Protocols for sample collection, storage, and measurements needed for the present study were approved by the Ethics Committee at the Osaka Medical College Hospital. This clinical research was conducted according to the Declaration of Helsinki principles. Under written informed consent, we collected brain tumor samples from patients who were subjected to surgical resection at the Department of Neurosurgery of Osaka Medical College during the period of 2008 to 2009.

All patients were subjected to craniotomy for tumor resection. Three hours prior to the surgical operation, patients were orally administered 5-ALA 20 mg/kg (Cosmo Bio). After the brain tumor bulk was exposed, 5-ALA–induced PpIX fluorescence was visualized with an operating microscope (OPMI-Pentero; Carl Zeiss). The target region was exposed to laser light with a peak wavelength of 405 nm, and PpIX fluorescence was detected at 630 nm through an optical filter. The intensity of the tumor fluorescence was evaluated independently by 2 neurosurgeons to ensure the objectiveness of fluorescence observations. Tumors with deep-red fluorescence clearly discerned from surrounding normal brain were classified as the "strong fluorescence" group. On the other hand, tumors without fluorescence were classified as the "no fluorescence" group. To avoid any ambiguity in the judgment of 5-ALA–induced fluorescence, tumors with pinky "vague fluorescence" were excluded from the present study.[5]

Tumor resection was completed 4–6 h after administration of 5-ALA. Following the surgical resection, each tissue specimen was divided into two samples. One sample was fixed with 10% formalin and embedded in paraffin for histological diagnosis and immunohistochemical studies, whereas the other sample was immediately frozen and stored in the dark at −80°C until qRT-PCR analysis was performed. All of the samples from a total of 19 patients were kept anonymous throughout the present study. Table 1 summarizes the clinical information for the brain tumor samples collected for this study.

Quantitative Real-time PCR Analysis of mRNA Levels

Total RNA was extracted from the frozen samples by the Magna Pure LC kit (Roche) according to the manufacturer's instructions. First strand cDNA was synthesized from the extracted RNA in a reverse transcriptase reaction by using the Transcriptor First-Strand cDNA Synthesis Kit (Roche Diagnostics).

Performance of qRT-PCR was with synthesized cDNA preparations to detect the mRNA levels of PEPT1, PEPT2, ALAS1, ALAS2, ALAD, HMBS, UROS, UROD, ABCB6, CPOX, PPOX, ABCG2, FECH, HIF-1, and HO-1. The primers used for the detection of those genes are listed in Table 2. The reaction was run in a Light Cycler (Roche Diagnostics) according to the Taqman assay protocol. The reaction conditions comprised a denaturation step (95°C for 10 min) and an amplification and quantification process repeated 45 times (95°C for 15 s and 60°C for 60 s). The data were analyzed by using the software of Light Cycler 3. The relative mRNA levels were calculated as a ratio of target gene to glyceraldehyde-3-phosphate dehydrogenase (GAPDH) by referring to the mRNA level of the *GAPDH* gene for each tumor sample.

Immunohistochemistry Analysis

The expression of CPOX and Ki-67 proteins in paraffin-embedded tumor sections was detected by immunohistochemical staining with the DAKO Envision + system. First, tumor-containing sections (5-μm thickness) were baked at 98°C for 40 min, deparaffinized in xylene, and rehydrated in graded concentrations of ethanol to distilled water. Heat-induced antigen retrieval was used. The sections were treated with 3% hydrogen peroxide in methanol to quench the endogenous peroxidase activity, which was followed by incubation with 1% bovine serum albumin to block the nonspecific binding of antibodies. As the first antibodies, we used anti-CPOX rabbit polyclonal antibody (Protein Tec 12211-1-AP) or anti–Ki-67 mouse monoclonal antibody (DAKO M7240). The sections were incubated with the first antibody (1:1200 dilution for Protein Tec 12211-1-AP or 1:100 dilution for DAKO M7240) at 37°C overnight. Thereafter, each section was incubated

Table 1. Summary of clinical samples from brain tumor patients

Sample Number	Diagnosis	Age	Sex	Ki-67 (%)	MRI (Gd-enhanced)	PpIX Fluorescence
1	Glioblastoma	17	Male	18	Strong/ring	No
2	Glioblastoma	76	Male	63	Strong/solid	No
3	Meta (lung)	66	Male	50	Strong/ring	No
4	Meta (breast)	51	Female	48	Strong/solid	No
5				58	Strong/solid	No
6	Meta (breast)	62	Female	52	Strong/solid	No
7	Meta (breast)	86	Female	32	Strong/ring	No
8	Meta (lung)	78	Female	23	Strong/solid	No
9	Meta (colon)	81	Male	84	Strong/ring	No
10	Meta (breast)	49	Female	15	Strong/solid	No
11	Glioblastoma	42	Male	12	Strong/ring	Strong
12	Glioblastoma	61	Male	5	Strong/ring	Strong
13	Glioblastoma	58	Male	42	Strong/ring	Strong
14	Glioblastoma	60	Female	15	Strong/ring	Strong
15	Glioblastoma	75	Male	50	Strong/ring	Strong
16	Glioblastoma	47	Male	30	Strong/ring	Strong
17	Glioblastoma	75	Male	20	Strong/ring	Strong
18	Meta (lung)	63	Female	11	Strong/ring	Strong
19	Meta (esophagus)	57	Male	81	Strong/ring	Strong
20	Meta (lung)	56	Male	36	Strong/solid	Strong

Abbreviation: Meta, metastatic brain tumor. Primary tumors are described in parentheses.

with horseradish peroxidase-labeled anti-rabbit immunoglobulin (Ig) G or anti-mouse IgG as the second antibody for detection of the CPOX or Ki-67 proteins, respectively. The negative controls were prepared in the same manner, but without the first antibodies.

Hematoxylin was used for nuclear counterstaining, whereas eosin was used as the cytoplasmic counterstaining agent, especially for immunostaining of the Ki-67 protein. Hematoxylin and eosin (H&E) staining was performed according to the standard procedure. Tissue areas were selected for immunohistochemical analysis based on visual alignment with the corresponding H&E-stained sections on slides. All of the samples were reviewed by 2 independent investigators who were blinded to the patients' clinical diagnosis results. Expression of the CPOX or Ki-67 proteins in the tissue area was quantified by counting the number of immunologically positive tumor cells and then calculating this number as a percentage against the total number of tumor cells within 3 high-power fields (magnification ×400; at least 200 tumor cells per 3 high-power fields) in the best-stained tumor area of each section. Cells with staining of CPOX and Ki-67 were interpreted as CPOX and Ki-67–expressing cells (%). The value used for statistical analysis was the average of the readings by the 2 counting investigators for each tumor.

Statistics

All statistical analyses were carried out with JMP version 8. The Wilcoxon test was performed to compare the mRNA levels of the genes tested as well as the percentages of cells positive for CPOX or Ki-67 in the immunohistochemical analyses between the "no fluorescence" and "strong fluorescence" groups. $P < .05$ indicates statistical significance. The best cutoff value for CPOX expression between none and strong fluorescence was calculated by analysis of receiver operating characteristics.

Results

Sample Collection

For 19 brain tumor cases, we examined 5-ALA–induced tumor fluorescence during surgical procedure by collecting a total of 20 tumor samples (Table 1). These included 10 tumor samples without 5-ALA–induced fluorescence (the no-fluorescence group) and 10 samples with strong fluorescence (the strong-fluorescence group). In the no-fluorescence group, 3 of the 10 samples were diagnosed as glioblastomas, and 7 were histologically diagnosed as metastatic brain tumors with primary tumors of the breast ($n = 4$), lung ($n = 2$), and colon ($n = 1$). Two samples (numbers 4 and 5) were obtained from the same patient who had a brain tumor metastasized from breast cancer (Table 1). In the strong-fluorescence group, 7 of its 10 samples were diagnosed as glioblastomas, and 3 were histologically metastatic brain tumors with primary tumors of the lung ($n = 2$) and esophagus ($n = 1$).

Preoperative Gadolinium-enhanced MRI Scanning and 5-ALA–induced Tumor Fluorescence

Preoperative gadolinium (Gd)-enhanced MRI scanning revealed strongly enhanced rings or solid tumor masses

Table 2. qRT-PCR primers to quantitatively measure the mRNA levels of the PEPT1, PEPT2, ALAS1, ALAS2, ALAD, HMBS, UROS, UROD, ABCB6, CPOX, PPOX, ABCG2, FECH, HIF-1, and HO-1 genes

Gene	F/R	Primer Sequence	Position	T_m
PEPT1	Forward	CCCTGAAGTGAAGGTGTTTGAAGATA	1772–1797	60.6
NM_005073	Reverse	GAATTGGCCCCTGACATGAA	2168–2188	59.3
PEPT2	Forward	CTACCACAATATGCCCTGGTTACA	1894–1917	58.8
NM_001145998	Reverse	GCCACTGAACTGTGCCACAA	2045–2064	59.3
ALAS1	Forward	GGATTCGAAACAGCCGAGTG	1371–1390	59.3
NM_000688	Reverse	GAAGGTGATTGCTCCAAACTCAT	1542–1564	58.3
ALAS2	Forward	AAGATGTGAAGGCTTTCAAGACA	419–441	60
NM_000032	Reverse	GGAAAATGGCTTCCTTAGGC	470–489	60
ALAD	Forward	CCTCGGTTCCAACCAACTGAT	157–177	59.8
NM_000031	Reverse	GATAGGCTGTATGTCATCAGGAACA	319–343	58.2
HMBS	Forward	CAAGGACCAGGACATCTTGGAT	835–856	58.9
NM_000190	Reverse	CCAGACTCCTCCAGTCAGGTACA	984–1006	59.2
UROS	Forward	TCAGCACTGCCTCTTCTATTTCC	668–691	58.7
NM_000375	Reverse	CTGGGTGTGCAACTGTCTGATAC	761–789	58.3
UROD	Forward	CGGGAGTGTGTGGGGAA	982–998	57.2
NM_000374	Reverse	AAGCAGACGTGAGTGTTTATGCA	1178–1200	58.6
ABCB6	Forward	CAGAAGGGCCGTATTGAGTTTG	2033–2054	59.6
NM_005689	Reverse	ATTGTCGGCGATGGTGTCA	2308–2326	59.5
CPOX	Forward	GGCGGAGATGTTGCCTAAGAC	401–421	59.7
NM_000097	Reverse	AATGCTCACCCCAGCCTTTT	709–728	59.5
PPOX	Forward	CAGGAGTCCTGGGAATCGTGTA	1251–1272	59.9
NM_000309	Reverse	TGCCTAGCTGACTCTAGTTTTTGC	1509–1533	58.1
FECH	Forward	GGAAATCCATTGTTCTCTAAGGC	1252–1274	57
NM_001012515	Reverse	CTAAATAACACCCTCTCCACATCG	1462–1485	57.8
ABCG2	Forward	CTAAGCAGGGACGAACAATCATC	1188–1210	58.8
NM_004827	Reverse	TCCTGCTTGGAAGGCTCTATG	1447–1467	58.2
HIF-1	Forward	GGCGCGAACGACAAGAA	420–436	58
NM_001530	Reverse	C AAAACCATCCAAGGCTTTCA	682–702	58.7
HO-1	Forward	GCTCAAAAAGATTGCCCAGAA	518–538	58.1
NM_002133	Reverse	TCACATGGCATAAAGCCCTACA	926–947	59.1

Abbreviations: F/R, forward or reverse primers; T_m, melting temperature.

with surrounding edema for all of the 19 brain tumor cases studied (Table 1). Figure 1 depicts representative results of the preoperative Gd-enhanced MRI scanning (left panels) as well as the photo-images of 5-ALA–induced tumor fluorescence (right panels) in brain tumors of two patients. The results of panels A and B are from 1 patient with a breast-originated metastatic brain tumor (sample number 6 belonging to the no-fluorescence group) and 1 with glioblastoma (sample number 20 belonging to the strong-fluorescence group), respectively. Those patients were administered 20 mg/kg of 5-ALA orally 3 hours prior to the surgical operation. The 5-ALA–induced tumor fluorescence was then visualized with a surgical OPMI-Pentero operation microscope, which revealed that tumor regions were exposed to laser light with a peak wavelength at 405 nm, and emission light was detected through a 630-nm bandpass filter. As clearly demonstrated, the glioblastoma (B) exhibited strong 5-ALA–induced PpIX fluorescence, whereas the metastatic brain tumor (A) did not. It is important to note that all the specimens

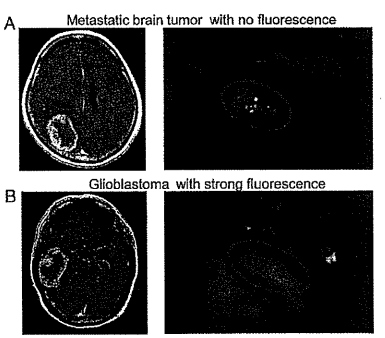

Fig. 1. Preoperative Gd-enhanced MRI scanning and 5-ALA-induced tumor fluorescence. Circular lines show the tumor location in operative view. (A) Metastatic brain tumor with no fluorescence. (B) Glioblastoma with strong fluorescence.

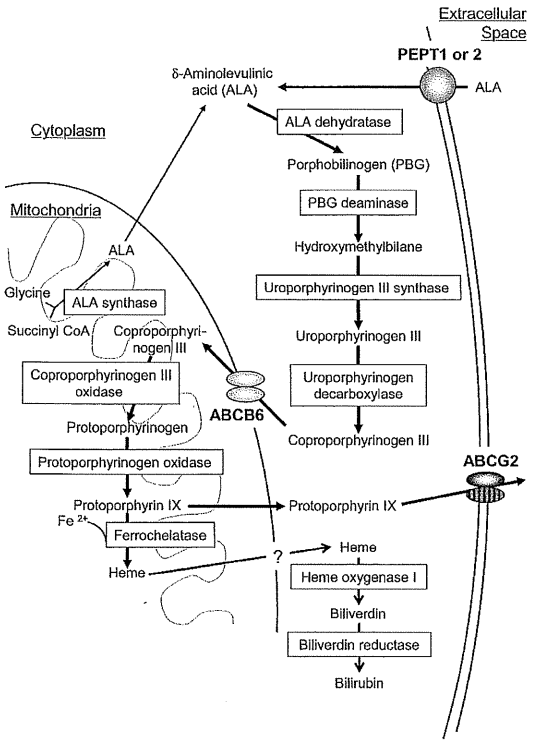

Fig. 2. Schematic illustration for the biosynthesis and catabolism of porphyrin and heme. Rectangles indicate the enzymes involved in porphyrin metabolism. Porphyrins are synthesized from glycine and succinyl Co-A via enzymatic reactions. Heme formed from porphyrin is catabolized to biliverdin by the microsomal enzyme heme oxygenase 1. Biliverdin is subsequently metabolized to bilirubin by biliverdin reductase. The ABC transporter ABCB6 is considered to be responsible for the import of coproporphyrinogen III into mitochondria, whereas ABCG2 transports porphyrins across the plasma membrane to maintain intracellular porphyrin homeostasis.

both with and without 5-ALA fluorescence exhibited strong Gd enhancement of MRI for the brain tumor cases treated in the present study (Table 1). This enhancement of MRI is ascribed to the disruption of the blood-brain barrier. In this context, we assumed that additional factor(s), besides disruption of the blood-brain barrier, could greatly affect the intensity of 5-ALA–induced fluorescence in brain tumors.

Semiquantitative Analysis of Gene Expression Levels by qRT-PCR

We extracted total RNA from the 20 tumor samples and measured the mRNA levels of genes encoding enzymes and transporters that are involved in the porphyrin-biosynthesis pathway (Fig. 2). The enzymes and transporters were oligopeptide transporters 1 and 2; 5-aminolevulinate synthases 1 and 2; 5-aminolevulinate dehydratase, hydroxymethylbilane synthase, uroporphyrinogen III synthase, uroporphyrinogen decarboxylase, CPOX, protoporphyrinogen oxidase, ferrochelatase, and the ABC transporters ABCB6 and ABCG2. In addition, the transcription factor HIF-1 was also measured by qRT-PCR, as it is critically involved in porphyrin transport and homeostasis under hypoxic conditions.[16] For the PCR-based semiquantitative measurements, we used the primer sets described in Table 2. The mRNA level of each gene was normalized by reference to that of the *GAPDH* gene.

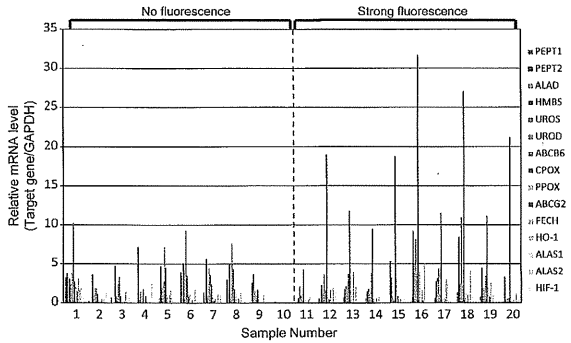

Fig. 3. The mRNA levels of the PEPT1, PEPT2, ALAS1, ALAS2, ALAD, HMBS, UROS, UROD, ABCB6, CPOX, PPO, FECH, ABCG2, and HIF-1 genes in individual tumor specimens.

Figure 3 shows the relative mRNA levels of those genes in the 20 tumor samples. While the profiles of mRNA levels varied among those samples, the mRNA levels of CPOX were commonly higher in the samples of the strong-fluorescence group than the levels in the no-fluorescence group. Figure 4A shows more clearly the difference in mRNA levels between the strong-fluorescence and no-fluorescence groups. The increase in CPOX mRNA level is remarkable in the strong-fluorescence group, showing an average increase of about 10-fold ($P = .0003$). The best cutoff value for CPOX expression levels that discriminates between the strong-fluorescence and no-fluorescence groups was calculated to be 4.3 (CPOX/GAPDH), as shown by a horizontal broken line in Figure 4B. These data strongly suggest that the upregulated expression of the CPOX gene is correlated with the intensity of tumor fluorescence induced by 5-ALA.

In addition to CPOX, mRNA levels of the ALAS1, UROS, PPOX, and FECH genes appeared to be higher in the strong-fluorescence group, whereas those of PEPT1, PEPT2, ABCB6, and ABCG2 were somewhat lower (Fig. 4A). However, there was no statistical significance between the strong-fluorescence and the no-fluorescence groups for these genes. It is interesting to note that the expression levels of PEPT1 and PEPT2, both 5-ALA influx transporters, seem to be downregulated in the strong-fluorescence group.

Expression Levels of CPOX Protein Measured by Immunohistochemical Staining

Since the qRT-PCR data suggested that the increased mRNA level of CPOX could be a key mechanism for the 5-ALA–induced tumor fluorescence, we used a CPOX-specific polyclonal antibody to examine CPOX protein expression by immunohistochemical staining for all of the 20 tumor samples. Figure 5 shows the results of H&E staining and CPOX immunohistochemical staining for glioblastoma and metastatic brain tumor samples in both the no-fluorescence and strong-fluorescence groups. Strong immunostaining with the CPOX antibody was observed in both glioblastoma and metastatic brain tumor samples in the strong-fluorescence group. Conversely, glioblastoma and metastatic brain tumors in the no-fluorescence group exhibited very weak immunostaining with the CPOX antibody.

The percentage of CPOX-positive cells was 0% to 50% (mean 19 ± 15.8) in brain tumor samples of the no-fluorescence group. In contrast, the percentage was 65% to 100% (mean 91.2 ± 11.5) in the strong-fluorescence group (Fig. 5B). The percentage of CPOX-positive cells was significantly higher ($P = .0001$) in the strong-fluorescence group than in the no-fluorescence group.

To gain further insight into a potential link between the proliferative capacity of brain tumors and the 5-ALA–induced tumor fluorescence, we immunohistochemically examined the expression of the proliferation marker Ki-67 in the tumor samples. The percentage of Ki-67–positive cells was 17.5% to 84% (mean $44.2 \pm 22.1\%$) in the no-fluorescence group and 5% to 81% (mean $30.2 \pm 23.1\%$) in the strong-fluorescence group. There was no statistically significant difference between the two groups, suggesting that the upregulation of CPOX gene expression was independent of the proliferative capacity of these brain tumors.

Discussion

Increased Expression of the CPOX *Gene and 5-ALA-induced Fluorescence in Malignant Brain Tumors*

In PDD and fluorescence-guided neurosurgery,[5–9] ALA is used for intraoperative labeling of the border regions